JCB Journal of Cell Biology

ARTICLE

# Prickle2 regulates apical junction remodeling and tissue fluidity during vertebrate neurulation

Miho Matsuda[1] and Sergei Y. Sokol[1]

**The process of folding the flat neuroectoderm into an elongated neural tube depends on tissue fluidity, a property that allows epithelial deformation while preserving tissue integrity. Neural tube folding also requires the planar cell polarity (PCP) pathway. Here, we report that Prickle2 (Pk2), a core PCP component, increases tissue fluidity by promoting the remodeling of apical junctions (AJs) in *Xenopus* embryos. This Pk2 activity is mediated by the unique evolutionarily conserved Ser/Thr-rich region (STR) in the carboxyterminal half of the protein. Mechanistically, the effects of Pk2 require Rac1 and are accompanied by increased dynamics of C-cadherin and tricellular junctions, the hotspots of AJ remodeling. Notably, Pk2 depletion leads to the accumulation of mediolaterally oriented cells in the neuroectoderm, whereas the overexpression of Pk2 or Pk1 containing the Pk2-derived STR promotes cell elongation along the anteroposterior axis. We propose that Pk2-dependent regulation of tissue fluidity contributes to anteroposterior tissue elongation in response to extrinsic cues.**

## Introduction

Epithelial tissue fluidity is defined as the ability of epithelia to deform in response to stimuli while preserving structural integrity (Atia et al., 2021; Farhadifar et al., 2007; Guillot and Lecuit, 2013; Mongera et al., 2018; Park and Fredberg, 2016; Wang et al., 2020). In developing vertebrate embryos, an initially flat embryonic epithelium has a high potential to deform. In response to physical or chemical cues, individual epithelial cells change their shape and neighbors in a highly organized anisotropic manner, leading to the formation of tissues or organs. Directional apical junction (AJ) remodeling is a key regulator of epithelial tissue deformation. However, the underlying mechanisms are largely unknown (David et al., 2014; Founounou et al., 2021; Kim et al., 2021; Kuriyama et al., 2014).

The *Xenopus* ectoderm is a good model for studying tissue fluidity during morphogenesis. At the onset of neurulation, the neuroectoderm (NE) is "fluid-like" with frequent cell intercalation and apical constriction, which are required for neural tube closure (NTC) (Baldwin et al., 2022b; Christodoulou and Skourides, 2022; Matsuda et al., 2023; Williams et al., 2014). In contrast, the nonneural ectoderm (future epidermis) is "solid-like," characterized by hexagonal packing and a low rate of cell intercalation. Notably, epithelia can reacquire "fluidity" during morphogenetic changes, allowing further deformation (Bocanegra-Moreno et al., 2023; Classen et al., 2005; Lawton et al., 2013; Mao and Wickström, 2024; Mitchel et al., 2020; Tetley and Mao, 2018). For example, the reduced fluidity of the embryonic ectoderm at the end of gastrulation is replaced by increased cell–cell rearrangements and apical domain heterogeneity during neurulation. Therefore, the spatiotemporal regulation of tissue and AJ fluidity is a hallmark of epithelial morphogenesis.

The planar cell polarity (PCP) pathway regulates the directionality of collective cell movements during morphogenesis. Originally defined in *Drosophila* genetic studies, core PCP components coordinate cell orientation in the tissue plane (Goodrich and Strutt, 2011; Humphries and Mlodzik, 2018; Peng and Axelrod, 2012). Vertebrate PCP is believed to be maintained by the feedback regulation of two complementary core protein complexes, Celsr–Vangl–Prickle (Pk) and Celsr–Frizzled (Fz)–Disheveled (Dvl), which are distributed at AJs on the opposite sides of the cell cortex (Aw and Devenport, 2017; Davey and Moens, 2017; Peng and Axelrod, 2012). In the vertebrate mesoderm, the core PCP pathway promotes mediolateral (ML) cell intercalation during convergent extension movements, leading to defects in embryonic axis elongation (Gray et al., 2011; Keller, 2002, 2012; Sokol, 1996; Wallingford et al., 2002). In addition to defects in axis elongation, mutations in the core PCP components result in neural tube abnormalities (Colas and Schoenwolf, 2001; Henderson et al., 2018; Montcouquiol et al., 2003; Williams et al., 2014). The PCP pathway was proposed to promote ML cell intercalations, extending the NE along the anteroposterior (AP) axis (Ybot-Gonzalez et al., 2007). PCP signaling may also involve defects in radial cell intercalations (Ossipova et al., 2015a) and apical constriction (Galea et al., 2021; Ossipova et al., 2015b), a reduction in the apical domain size that is essential for neural

[1]Department of Cell, Developmental and Regenerative Biology, Icahn School of Medicine at Mount Sinai, New York, NY, USA.

Correspondence to Sergei Y. Sokol: sergei.sokol@mssm.edu; Miho Matsuda: miho.matsuda@mssm.edu.







https://doi.org/10.1083/jcb.202407025

plate folding. Taken together, these studies suggest that PCP signaling may control tissue fluidity during epithelial morphogenesis.

The core PCP components are functionally linked to the actomyosin cytoskeleton. The Fz-Dvl complex binds RhoGEF and Daam1, a formin family protein that activates RhoA in the cell cortex (Habas et al., 2001; Nishimura et al., 2012). The Fz-Dvl complex therefore promotes the formation of supracellular actomyosin cables that help bend the neural plate (McGreevy et al., 2015; Nishimura et al., 2012; Röper, 2013). The Vangl-Pk complex is enriched at the anterior cell edge in various vertebrate models (Butler and Wallingford, 2018; Ciruna et al., 2006; Devenport and Fuchs, 2008; Mancini et al., 2021; Ossipova et al., 2015c; Yin et al., 2008). However, the cellular targets of Vangl and Pk that mediate tissue deformation largely remain to be identified.

In this study, we investigate the role of Prickle2 (Pk2) in AJ remodeling and tissue fluidity control during neurulation. Consistent with its presumed function as a core PCP protein, Pk2 is polarized at the anterior AJ of *Xenopus* neuroepithelial cells, and Pk2 morphants exhibit NTC defects (Butler and Wallingford, 2018). The same study revealed a correlation between Pk2 and actomyosin enrichment in shrinking AJs; however, the underlying mechanism and causation remain unclear. Here, we show that Pk2 knockdown (KD) in the NE, a fluid-like epithelium, attenuates AJ elongation and shrinkage. Conversely, Pk2 overexpression (OE) in the gastrula ectoderm, a solid-like epithelium, promotes AJ elongation and shrinkage, inhibiting hexagonal cell packing, a hallmark of the ectoderm at the end of gastrulation. This activity of Pk2 is unique and involves an evolutionarily conserved Ser/Thr-rich region (STR) of the protein. It also requires Rac1 activity and is accompanied by increased C-cadherin and actomyosin dynamics at AJs. Importantly, the effects of Pk2 on AJ remodeling are anisotropic in the NE and induce preferential elongation of cells along the AP axis. We propose that Pk2 increases epithelial tissue fluidity, leading to an enhanced response of the epithelia to anisotropic cues from the environment.

## Results

### Pk2 depletion decreases the rate of AJ remodeling in the NE

We assessed the role of Pk2 in AJ remodeling and tissue fluidity in *Xenopus* NE, a fluid-like epithelium characterized by intensive AJ remodeling, cell intercalation, and apical domain variability (Baldwin et al., 2022a; Christodoulou and Skourides, 2022; Matsuda et al., 2023; Williams et al., 2014). To unilaterally deplete Pk2 in the NE (Fig. 1 A), a previously characterized splicing-blocking morpholino (MO) (Butler and Wallingford, 2015, 2018; Devitt et al., 2024; Shindo et al., 2019) was coinjected with a lineage tracer RNA into one dorsal blastomere at the four- to eight-cell stage. Unilateral KD minimizes AP axis elongation defects, allowing a comparison of the behaviors of morphant and wild-type NE cells in the same embryo (Fig. 1 A). We assessed changes in AJs, cells, and cell–cell arrangements in the posterior NE close to the brain–spinal cord border, where ∼20% of cells per hour intercalate and replace mediolaterally oriented junctions with anteroposteriorly oriented junctions (Butler and Wallingford, 2018).

Pk2 KD disrupted NTC as reported previously (Fig. 1 B and Video 1) (Butler and Wallingford, 2018). The apical domain of Pk2-KD NE cells remained large (Fig. 1, B and C), suggesting defects in apical constriction. In *Drosophila*, medioapical actomyosin pulses have been implicated in apical constriction during epithelial folding (Martin et al., 2010). In the *Xenopus* NE, medioapical actomyosin increases in apically constricted cells, and the reduced medioapical F-actin correlates with apical constriction defects (Baldwin et al., 2022a). Consistent with these findings, the Pk2 KD NE presented a loss of apically constricted cells and a loss of cells with strong medioapical F-actin enrichment (Fig. S1, A–E). These results suggest reduced actomyosin contractility in Pk2 KD cells.

PCP signaling controls convergent extension in the NE (Ybot-Gonzalez et al., 2007). In *Xenopus* embryos, mediolaterally oriented cell intercalation extends the NE anteroposteriorly, followed by apical constriction, which folds the neural tube (Baldwin et al., 2022a; Christodoulou and Skourides, 2022). Therefore, we next tested the effects of Pk2 KD on cell intercalation. Time-lapse imaging revealed that Pk2 KD did not reduce the frequency of T1 transitions (white circles in Fig. 1, D–H and Video 2). It also did not affect the orientation of T1 transitions (a total of 277/277 ML-to-AP intercalation events in three Pk2 KD embryos). However, the elongation of newly formed AP junctions slowed after the resolution of T1 junctions (double arrows in Fig. 1, D–G). Tracking of randomly selected junctions revealed that Pk2 KD generally reduces the rates of elongation and shrinkage of AJs (Fig. 1, I and J). These results suggest that Pk2 is required for the efficient remodeling of AJs and that this may also contribute to the failure of apical constriction in the Pk2 KD NE.

### Posterior NE cells do not extend along the AP axis after Pk2 depletion

Another change in the Pk2 KD NE is the loss of cell reorientation. Wild-type cells were more mediolaterally oriented in the early neurula and progressively acquired AP orientation during neural fold formation (myrRFP in Fig. 2, A and B; and Video 3). Pk2-depleted cells retained the ML orientation (myrGFP+Pk2MO in Fig. 2, A and B; and Video 3). We confirmed the defects in cell reorientation in the phalloidin-stained embryos (Fig. S1, G–G‴ and I). Although Pk1 depletion disrupted NTC (Fig. S1 H), Pk1-KD cells reoriented in the NE (Fig. 1, K; Fig. S1, H and J; and Video 4). Similarly, Vangl2 KD in the NE did not alter cell reorientation despite strong NTC defects (Matsuda et al., 2023). These results indicate that the observed cell orientation defect is specific to Pk2.

To further define defects in AJ remodeling, changes in AJ length and orientation were analyzed in more detail (Fig. 2, C–G). As shown previously (Baldwin et al., 2022a; Christodoulou and Skourides, 2022), AP junctions were longer than ML junctions in the control NE (Fig. S1 F). Individual AP junctions preferentially elongated, whereas ML junctions shrank (Fig. 2, F and H). Our analysis also revealed that individual AJs change orientation (Fig. 2 F), contributing to the ML-to-AP reorientation of cells. In the Pk2-depleted NE, ML junctions were longer than AP junctions (Fig. S1 F). The elongation and shrinkage of AP and ML junctions

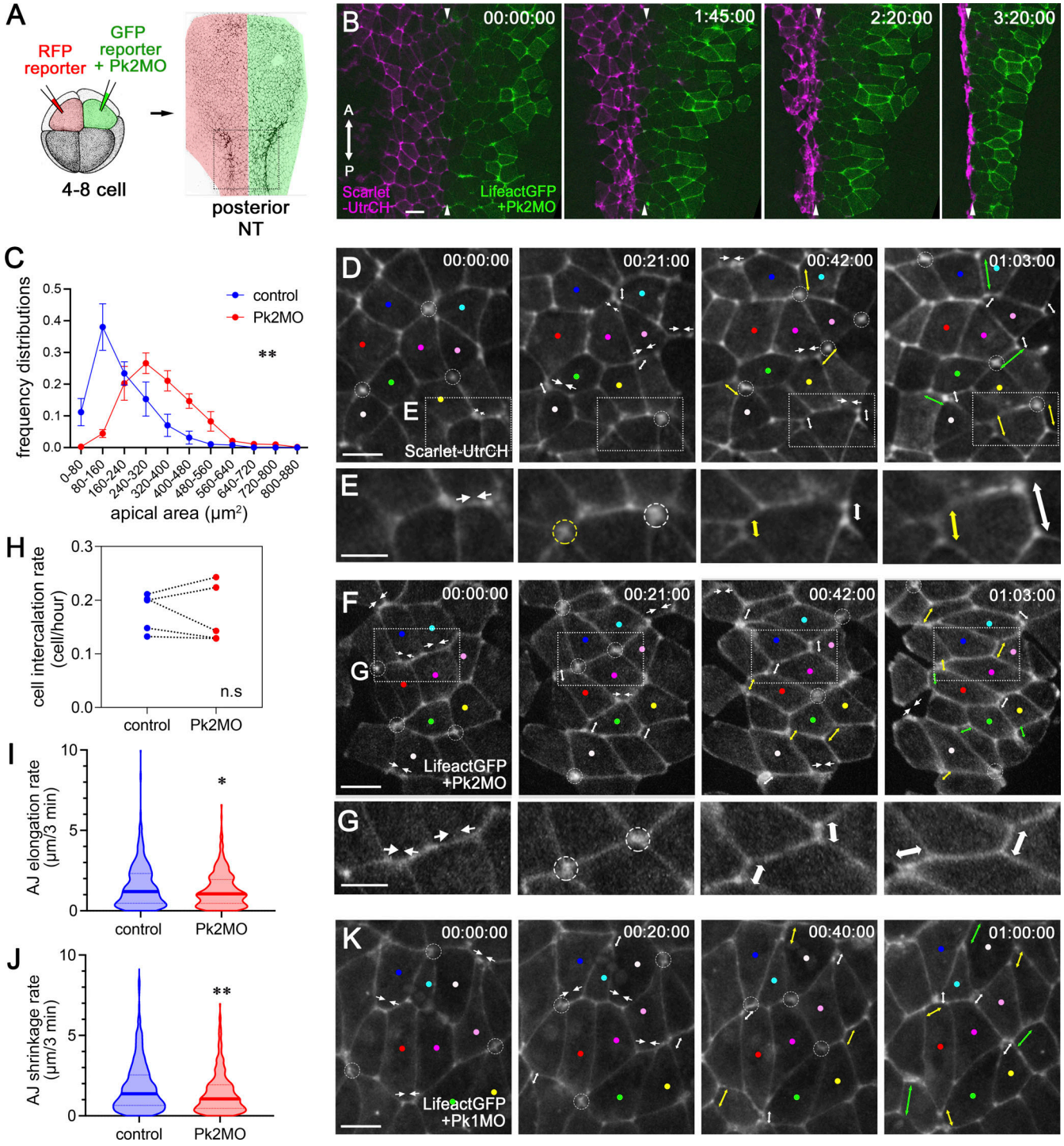


Figure 1. **Pk2 KD in the *Xenopus* NE attenuates AJ remodeling. (A)** Experimental scheme. Pk2 MO was injected with GFP reporter RNA into one dorsal-animal blastomere (green) at the four- to eight-cell stage. RFP reporter RNA was injected into the other dorsal-animal blastomere (red) as a control. The superficial layer of the posterior NE near the brain–spinal cord border was imaged. **(B)** Representative images of the control (Scarlet-UtrCH) and Pk2 MO (Lifeact-GFP) NEs from Video 1. Imaging was initiated at stage 15 with 5-min intervals and a duration of 3 h 40 min. Arrowheads indicate the midline. A: anterior. P: posterior. **(C)** Frequency distribution histogram of the apical domain size in the posterior NE in control and Pk2 MO embryos. Stage 15–16 embryos were stained with phalloidin. Five embryos per group were used. The total number of cells was as follows: $n$ = 1,098 (control) and $n$ = 1,168 (Pk2 MO). **(D–G)** Representative control (D and E) and Pk2 KD (F and G) images of stage 15–16 NEs from Video 2. The rectangular areas in D and F are enlarged in E and G. The colored dots represent cell tracking. The paired inward white arrows show shrinking AJs before T1 transition. The white circles represent T1 junctions. The white double arrows show the elongation of newly formed AJs after the T1 transition. The yellow circle represents four-cell junctions after cytokinesis. The yellow double arrow represents newly formed AJs after cytokinesis. **(H)** Frequency of T1 transition was compared between the control (blue) and Pk2 MO (red) sides of NEs in the same embryos. The dots represent the average frequency of T1 transition in individual embryos paired by a line. Five embryos per group were used. **(I and J)** Rates of AJ elongation (I) and AJ shrinkage on the control and Pk2-KD sides of NEs. A total of 312 AJs (control) and 285 AJs (Pk2 KD) were

randomly selected from three embryos. The bold and thin lines represent the medians and quartiles, respectively. **(K)** Representative still images of Pk1-KD NEs from Video 5. Imaging was initiated at stages 15–16 with 5-min intervals and a duration of 1 h 45 min. A: anterior. P: posterior. Statistical significance was determined as follows: the Mann–Whitney test was used to compare the mean ranks of the apical domain size (C). Paired Student's *t* test (two-sided) was used to compare the means of the cell intercalation rates. Data distribution was assumed to be normal, but this was not formally tested (H). The Mann–Whitney test was used to compare the mean ranks of AJ elongation (I) and shrinkage (J). *P < 0.05, **P < 0.01. n.s., not significant. Scale bars: 20 µm.

had similar frequencies (Fig. 2 H; and Fig. S1, K and L). These results suggest that Pk2 is required for the orientation-dependent control of AJ behavior.

In addition to AJ shrinkage and apical constriction, actomyosin contractile force has been reported to be important for AJ elongation in neighboring cells. During *Drosophila* AP axis elongation, paired pulsatile apical actomyosin at two opposite sides of T1 junctions was proposed to generate a pulling force, elongating newly formed AJs (Collinet et al., 2015; Finegan et al., 2019; Uechi and Kuranaga, 2019; Yu and Fernandez-Gonzalez, 2016). If a similar mechanism operates in *Xenopus* NE cells, the reduced actomyosin force in Pk2 KD cells may attenuate the extension of newly formed AP junctions. To test the effects of Pk2 KD on actomyosin, time-lapse imaging was conducted in embryos coexpressing sf9-mNeonGreen and Scarlet-UtrCH, which are live probes for nonmuscle heavy chain IIA and F-actin (Burkel et al., 2007; Hashimoto et al., 2015; Vielemeyer et al., 2010).

In the wild-type NE, sf9 preferentially accumulated in tricellular vertices, in which three or more cells meet (arrowheads in Fig. S2 A). During T1 transition (circles in Fig. S2 B), a pair of sf9-positive crescent-shaped actomyosin networks formed at the anterior and posterior sides of T1 junctions (arrowheads in Fig. S2, B and C; and Video 5), and newly formed AJs elongated between two sf9 crescents (double arrows in Fig. S2, B and C). These actomyosin networks (schematics in Fig. S2 C) are similar to those observed at T1 junctions in *Drosophila* embryos (Collinet et al., 2015; Finegan et al., 2019; Uechi and Kuranaga, 2019; Yu and Fernandez-Gonzalez, 2016). F-actin levels also increased at T1 junctions (arrows in Fig. S2, B and C); however, the current image resolution was not sufficient to separate F-actin networks in individual cells. In the Pk2 KD NE, medioapical actomyosin was pulsatile (Video 5). Pk2 KD did not affect the formation or spatial localization of sf9 crescents at T1 junctions (arrowheads in Fig. S2, D and E; and Video 5) (56/62 T1 junctions in wild type and 56/63 T1 junctions in Pk2 KD, three embryos each), although additional quantification may be necessary to fully evaluate the effects of Pk2 KD on actomyosin. Nevertheless, these observations suggest that reduced actomyosin contractility in tricellular vertices may not be the only reason for attenuated AJ elongation in Pk2 KD cells.

### Pk2 overexpression inhibits hexagonal cell packing in *Xenopus* ectoderm

We next asked whether Pk2 activity in facilitating AJ remodeling is specific for the NE. The superficial ectoderm in *Xenopus* gastrula contains well-organized AJs and apical–basal polarity (Cardellini et al., 2007; Fesenko et al., 2000). Importantly, the ectoderm is hexagonally packed at the end of gastrulation (control in Video 6), a hallmark of reduced tissue fluidity (Classen et al., 2005; Farhadifar et al., 2007). In early gastrula (00:00 h in Fig. 3 B), ectodermal cells were diverse in size and shape (control in Fig. 3, G and J) with fewer linear cell–cell boundaries (control in Fig. 3 I). At the end of gastrulation (stage 12, 04:55 h in Fig. 3, C, G, I, and J), the cells became more uniform in size (control in Fig. 3 G) and more hexagonal in shape (control in Fig. 3 J) and had more linear junctions (control in Fig. 3 I).

Pk2 maternal and zygotic transcripts are broadly expressed in *Xenopus* gastrula (https://www.Xenbase.org). We used gain-of-function approaches to test whether Pk2 OE increases AJ and tissue fluidity in this solid-like embryonic ectoderm system (Fig. 3 A). Compared with the wild-type control ectoderm, Pk2 OE in early gastrula (00:00 h in Fig. 3 C) did not affect the variability of the apical domain size (Fig. 3 G), AJ linearity (Fig. 3 I), or the number of neighbors (Fig. 3 J). However, Pk2 OE cells continued to exhibit apical domain variability (04:55 h in Fig. 3, C, G, I, and J; and Video 6), accompanied by increased lateral membrane dynamics (Fig. 3, D–F and Video 7) and more frequent cell intercalations (Fig. 4, A–C). These results suggest that Pk2 increases tissue fluidity, inhibiting hexagonal packing. This finding is complementary to the Pk2 morphant phenotype in the NE.

### Pk2 overexpression promotes AJ remodeling in the ectoderm

Dynamic remodeling of AJs increases tissue fluidity (Pinheiro and Bellaïche, 2018). To assess the direct effects of Pk2 OE on junction remodeling, we tracked changes in AJ length in non-mitotic cells (Fig. 4, D and E) and in newly formed AJs between two daughter cells after cytokinesis (double arrows in Fig. S3, A and B). In both cases, Pk2 OE accelerated AJ elongation and shrinkage (Fig. 4, F–I and Fig. S3 C). Notably, the orientation of AJ remodeling was random in the gastrula ectoderm, and Pk2 OE did not affect directionality (Fig. S3 E). The mitotic rate was similar between the Pk2 OE and control ectoderms (Fig. S3 D), excluding the potential effect of cell division on increasing tissue fluidity (Devany et al., 2021; Firmino et al., 2016; Matoz-Fernandez et al., 2017; Ranft et al., 2010). These results indicate that Pk2 promotes AJ remodeling, increasing tissue fluidity in the gastrula ectoderm.

Cadherin turnover is important for the dynamic remodeling of cell junctions (Kowalczyk and Nanes, 2012). To test AJ dynamics more directly, time-lapse imaging of C-cadherin was conducted. In the Pk2 OE ectoderm, the distribution of YFP-C-cadherin was less uniform at bicellular junctions (BJs) (Fig. 5, A–C and Video 8). C-cadherin puncta in the cytoplasm indicate increased endocytosis of C-cadherin (arrowheads in Fig. 5 B). In the fluorescence recovery after photobleaching (FRAP) assay (Fig. 5, D–G), the increased fraction of C-cadherin fluorescence signals was recovered 80 s after photobleaching (Fig. 5 F). The average recovery of C-cadherin was faster in the Pk2 OE

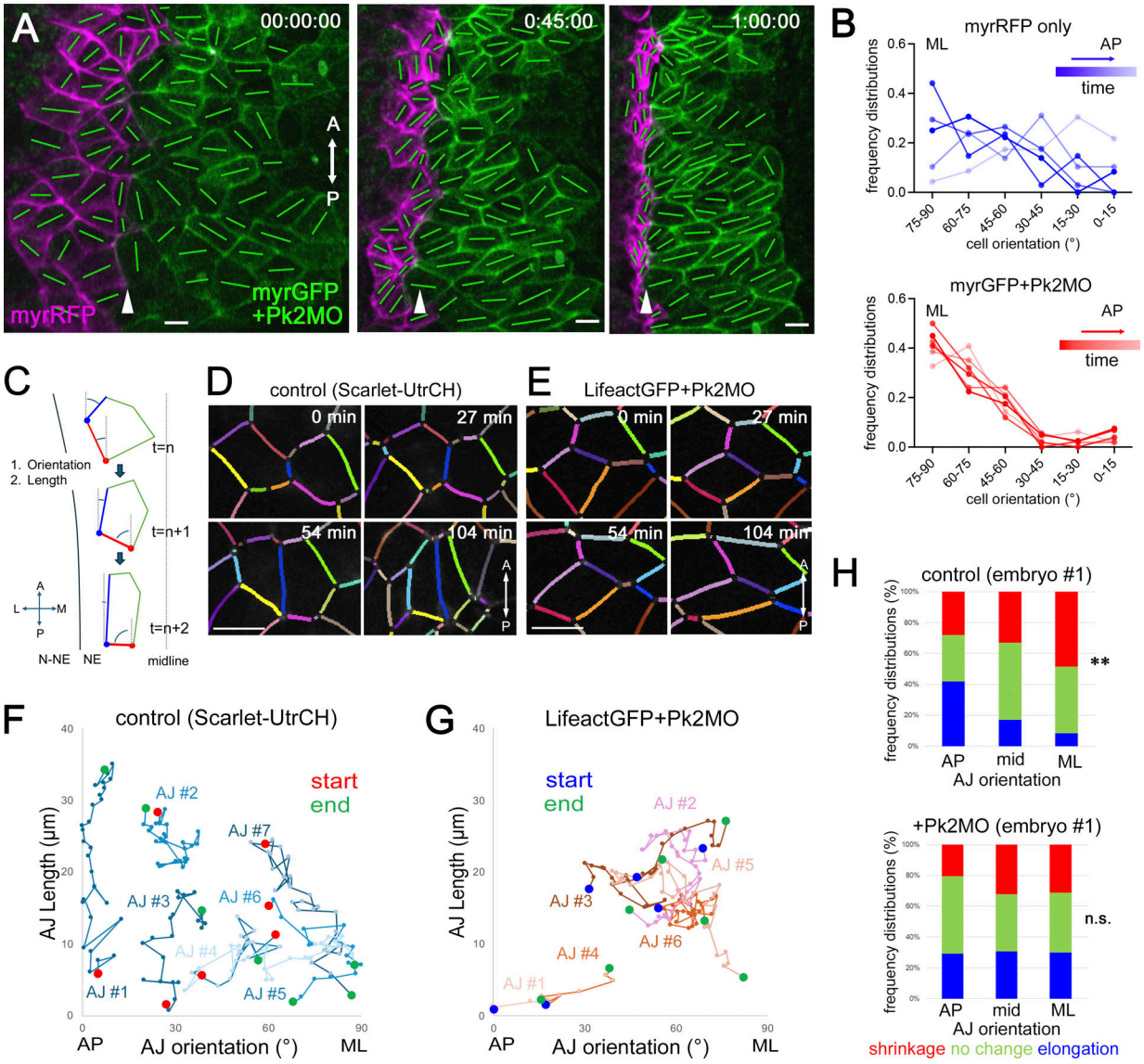


Figure 2. **Effects of Pk2 depletion on AJ orientation in the NE. (A)** Still images from time-lapse imaging of the control (myrRFP) and Pk2-KD (myrGFP) NEs from Video 3 with a duration of 1 h 12 min and 3-min intervals. Imaging was initiated at stages 15–17. The green lines represent the cell orientation. A: anterior. P: posterior. The white arrowhead indicates the presumed midline. **(B)** Representative frequency distribution histogram of cell orientation in the control (blue) and Pk2 KD (red) NEs from Video 3. The darker color represents NEs at earlier stages. Circular angles 0 and 90 correspond to the AP and ML axes, respectively. **(C)** Scheme of the AJ quantification method used in Fig. 2, F–H and Fig. 10, C–E. The orientation and length of individual AJs were quantified frame by frame. **(D and E)** Representative images of AJ tracking in the wild-type control (D) and Pk2-KD (E) NEs. **(F and G)** Representative 2D plot of AJ length and orientation changes in the control (F) and Pk2 KD (G) NEs, which were tracked for 1 h and 28 min. X axis: AJ orientation. Y axis: AJ length. Large red (F) or blue (G) dots indicate AJs before tracking. Large green dots indicate AJs at the end of tracking. The plots include seven control AJs (F) and six Pk2 MO AJs from one embryo (G). **(H)** Quantification of changes in AJ length in the control and Pk2 MO NEs. 17 AJs (control) and 15 AJs (Pk2 KD) were randomly selected from time-lapse images of one embryo. Changes in AJ length were categorized as follows: elongation (blue, ≥0.8 μm/3 min), shrinkage (red, less than or equal to −0.8 μm/3 min), and no change (green, −0.8< and <0.8 μm/3 min). Based on orientation, AJs were categorized into AP (≤30° from the AP axis), ML (≤30° from the ML axis), and mid (30–45° from either the AP or ML axes). The two-sample Kolmogorov–Smirnov test was used to compare distributions of AJ length changes between AP and ML junctions. The original numerical data were used for statistical analysis. The total number of AJ length changes was 353 (control) and 595 (Pk2 KD). The same analysis was conducted for two other embryos (Fig. S1, K and L). **P < 0.01, n.s., not significant. Bars: 20 μm.

ectoderm (Fig. 5 G). Notably, C-cadherin recovery was highly variable in the Pk2 OE ectoderm (Fig. 5, E and F). We observed that the C-cadherin fluorescence intensity decreased or exceeded the level observed before photobleaching (Fig. 5 D). The constant drift in the baseline fluorescence of C-cadherin (Fig. 5 C) appears to contribute to the inconsistent recovery of C-cadherin. Taken together, these results suggest increased turnover of C-cadherin, which is consistent with increased AJ dynamics in the Pk2 OE ectoderm.

### Pk2 OE promotes AJ remodeling at tricellular junctions (TCJs)

TCJs are hotspots of AJ remodeling and actomyosin tension and contain AJ and actomyosin components and TCJ-specific proteins (Bosveld et al., 2018; Finegan et al., 2019; Letizia et al., 2019;

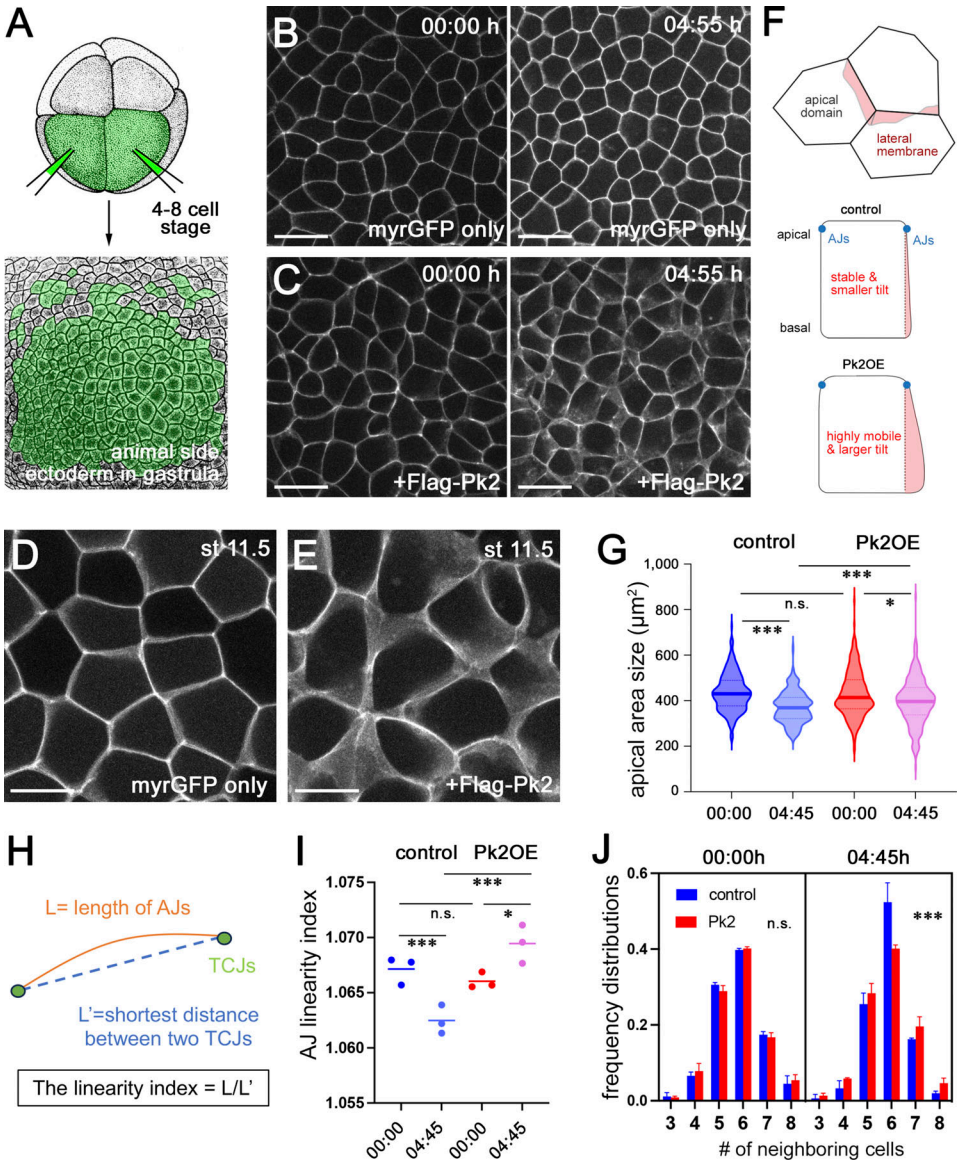


Figure 3. **Pk2 inhibits hexagonal packing in the gastrula ectoderm. (A)** Scheme of the experiment. Flag-Pk2 RNA was coinjected with GFP reporter RNA into two ventral blastomeres at the four- to eight-cell stage. Time-lapse imaging of the animal superficial ectoderm was initiated at stage 10. **(B and C)** Snapshot images of gastrula ectoderm expressing myrGFP only (B) and myrGFP with Flag-Pk2 (C) from Video 6. Left: 0 h. Right: 4 h 55 min. **(D–F)** Higher resolution snapshot images of ectoderms expressing myrGFP only (D) or with Flag-Pk2 (E) from Video 7. Imaging was initiated at stage 11.5. Unpigmented albino embryos were used to highlight myrGFP fluorescence signals from the lateral membrane, which are shown in red in the schematic diagram (F). **(G–J)** Quantification of hexagonal cell packing. Pigmented wild-type embryos were used for segmentation and quantification. Cell packing was assessed by apical domain size heterogeneity (G), AJ linearity (I), and the number of neighboring cells (J). Schematic of AJ linearity quantification (H). The actual length of the AJs is divided by the shortest distance between two vertices (L/L'). Dots represent the values of average AJ linearity in individual embryos (I). The lines correspond to the average values of three embryos. (J) Frequency distribution histogram of the number of neighboring cells. Original numerical data were used for statistical analysis in G and I. The Kolmogorov–Smirnov test was used to compare distributions in G. One-way ANOVA was used to compare the means of three or more groups in I. The Bonferroni correction was used for pairwise multiple comparisons. The chi-square test was used in J. The total number of cells or AJs scored in G–J was as follows: 576 cells and 1,127 AJs (myrGFP control, 00:00 h); 672 cells and 1,169 AJs (myrGFP control, 4:55 h); 724 cells and 1,360 AJs (myrGFP+F-Pk2, 00:00 h); and 764 cells and 1,355 AJs (myrGFP+F-Pk2, 4:55 h). Three embryos per group were used. *P < 0.05, **P < 0.01, ***P < 0.001, n.s., not significant. Scale bars: 50 μm (B and C) and 25 μm (D and E).

Uechi and Kuranaga, 2019; Vanderleest et al., 2018). TCJs are constantly remodeled; for example, E-cadherin levels at TCJs oscillate coordinately with changes in the apical domain size (Vanderleest et al., 2018). During AJ length changes, vertices at each end of BJs displace asymmetrically, and the displacement of vertices correlates with the increased fluctuation of E-cadherin (Huebner et al., 2021). In the gastrula ectoderm, Pk2 OE did not change the average abundance of C-cadherin (Fig. 5 H, bold lines in Fig. 5 I); however, it increased the variability of C-cadherin levels among TCJs (Fig. 5 I) and the fluctuation at individual TCJs (Fig. 5, J and K). These results suggest that Pk2 promotes C-cadherin dynamics at TCJs.

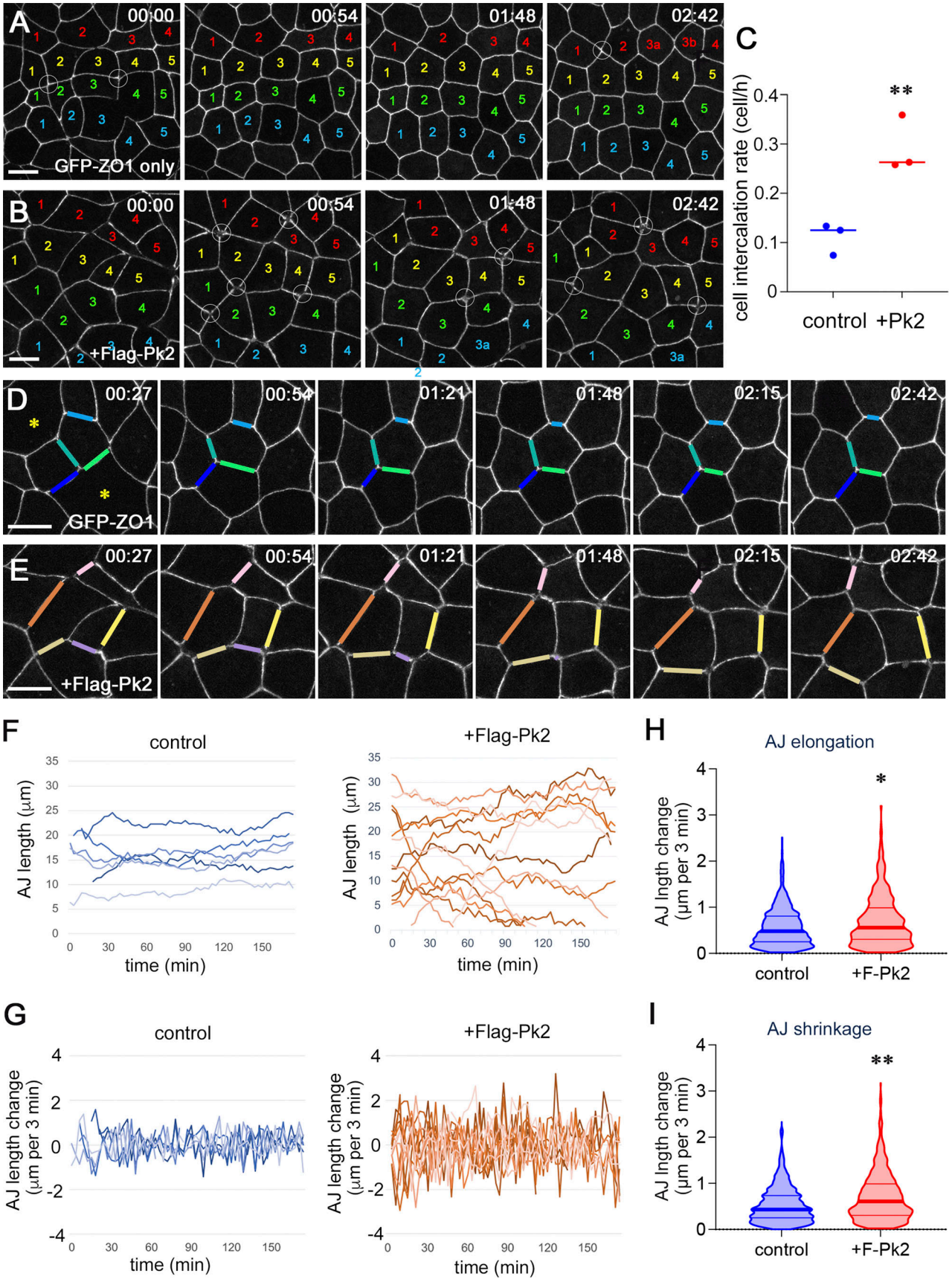


Figure 4. **Pk2 promotes AJ remodeling and cell intercalation in the gastrula ectoderm. (A and B)** Representative snapshot images of *Xenopus* gastrula ectoderm. GFP-ZO1 only (A) and GFP-ZO1 with Flag-Pk2 (B). Time-lapse imaging was initiated at stage 11. The white circles indicate T1 junctions. **(C)** Rate of

cell intercalation in the control or Pk2 ectoderm. Individual dots represent the average rates of cell intercalation in individual embryos. Unpaired Student's *t* test (two-sided) was used to compare the means. Data distribution was assumed to be normal, but this was not formally tested. Three embryos per experimental group were used. The total number of cells was as follows: *n* = 73 (control); *n* = 114 (Flag-Pk2). **(D and E)** Representative images of AJ tracking in control GFP-ZO1–only (D) or GFP-ZO1 with Flag-Pk2 OE (E) ectoderms. Asterisks indicate cell division. **(F)** Representative changes in AJ length. The plots included 6 AJs (control) and 14 AJs (+Flag-Pk2) from one embryo. **(G)** Calculated rates of AJ length change on the basis of data in F. **(H and I)** Rates of AJ elongation (H) and shrinkage (I) on the basis of 2 h and 42 min' tracking of 30 AJs (control) and 34 AJs (+F-Pk2). AJs were randomly selected from three embryos per group. The total number of AJ length changes in H and I was as follows: *n* = 1,836 (control); *n* = 1,729 (+F-Pk2). The bold and thin lines represent the medians and quartiles, respectively. The Mann–Whitney U test was used to compare the mean ranks. *P < 0.05, **P < 0.01. Scale bars: 20 µm.

Next, we asked whether Pk2 OE specifically affects C-cadherin or TCJ dynamics in general. Tricellulin is a tricellular tight junction protein essential for the structural integrity and barrier functions of TCJs (Bosveld and Bellaïche, 2020; Ikenouchi et al., 2005). Compared with the wild-type tissue (Fig. 5, L–M′), the ectoderm overexpressing Pk2 presented more variable (Fig. 5 P) and overall reduced levels of tricellulin (Fig. 5 O) at the TCJs, which was mislocalized to the BJs more frequently (arrowheads in Fig. 5, L–N) and increased the variability of fluorescence signals at BJs (Fig. 5 Q). These results suggest a general change in TCJs in response to Pk2.

Anisotropic actomyosin network formation has been reported at tricellular vertices during junction remodeling in elongating tissues (Collinet et al., 2015; Finegan et al., 2019; Rauzi et al., 2008, 2010; Uechi and Kuranaga, 2019). We tested actomyosin dynamics in the Pk2 OE ectoderm and observed changes in the spatial distributions of F-actin and nonmuscle myosin II (NMII) in tricellular vertices (Fig. S4 and Video 9). In the wild-type ectoderm (Fig. S4 A), coherent NMII- and F-actin–positive puncta were observed near the center of the TCJs (arrows in Fig. S4, A-a and C). In the Pk2 OE ectoderm, NMII puncta split into two to three separable structures with variable sizes and intensities (arrowheads in Fig. S4, B-b and b′; and Fig. S4 C), reducing overall actomyosin abundance at TCJs (Fig. S4, D and E). The pattern and number of NMII puncta at TCJs varied over time in the Pk2 OE ectoderm (Video 9). These results provide further evidence that Pk2 promotes dynamic TCJ remodeling.

### The STR of Pk2 is required for Pk2-induced increases in tissue fluidity

To determine the domains of Pk2 required for increased tissue fluidity, Pk2 deletion mutants (Fig. 6 A) were overexpressed in the gastrula ectoderm. Hexagonal cell packing was assessed by AJ linearity (Fig. 6 H), the variability in junction length (Fig. 6 I), and the number of neighbors (Fig. 6 J). Three domains were required to inhibit hexagonal packing. First, the C-terminal CAAX motif was required (Pk2ΔC30 in Fig. 6, G–J), a domain that mediates the membrane localization of Pk proteins (Fig. S5 N) (Cho et al., 2015). Second, it requires the Vangl-binding domain (VBD) (Butler and Wallingford, 2015; Jenny et al., 2003) (Pk2ΔVBD in Fig. 6, F and H–J), even though Pk2ΔVBD was localized at AJs (Fig. S5 M). Although Vangl2 OE alone did not inhibit hexagonal packing (Fig. S5, E and G–I), our finding that Pk2ΔVBD is inactive suggests that Pk2 cooperates with Vangl2 at AJs for full activity. The third required domain was the STR (Pk2ΔSTR in Fig. 6, D and H–J). The STR is an evolutionarily conserved domain among vertebrates Pk1 and Pk2, but it is absent in invertebrate Pk and vertebrate Pk3 (Fig. S5, A and B). We confirmed that Pk2ΔSTR localized at AJs in the gastrula ectoderm (Fig. S5 K). Other regions of Pk2, such as C4, were not required for AJ localization (Fig. S5 L) or the inhibition of hexagonal packing (Fig. 6, E and H–J).

### The STR is responsible for the functional differences between Pk1 and Pk2 in AJ remodeling

Previous studies have implicated Pk1 in cell motility and F-actin reorganization (Carreira-Barbosa et al., 2003; Huang and Winklbauer, 2022; Tao et al., 2009; Veeman et al., 2003) through interactions with GEFs and GAPs for Rho family small GTPases (Daulat et al., 2019; Zhang et al., 2016; Zhang and Wrana, 2018). ARHGAP21/23, GTPase-activating proteins for RhoA, bind Pk1 via a region including the STR, inactivate RhoA, and are proposed to regulate the formation of actin-rich protrusions during mammalian cell migration in vitro (Zhang et al., 2016). In our assays, Pk1 KD in the NE disrupted NTC (Fig. S1 H); however, Pk1 KD cells reoriented from the ML to the AP direction (Fig. S1 J). Pk1 OE did not inhibit hexagonal cell packing in the gastrula ectoderm (Fig. 7, C and I–K). However, mosaically expressed Pk1 induced the formation of concave cells with protrusion-like structures adjacent to TCJs (arrowheads in Fig. S6 B). In contrast, mosaic Pk2 OE cells had a convex shape (Fig. S6 C). The mechanisms underlying these morphological changes are not known, but differences in cell adhesion or cortical tension between neighboring wild-type and Pk OE cells may contribute to these changes. These observations revealed distinct activities of Pk1 and Pk2 in AJ remodeling and cell shape regulation.

To determine the domain responsible for the functional difference between Pk1 and Pk2, chimeric Pk1 and Pk2 proteins (Fig. 7 A) were expressed in the gastrula ectoderm. First, the C-terminal half of Pk2 conferred the ability to promote tissue fluidity to Pk1 (Pk1N-Pk2C in Fig. 7, D and I–K). Pk2N-Pk1C had the opposite effect (Pk2N-Pk1C in Fig. 7, G and I–K). The STRs contain amino acids conserved among both Pk1 and Pk2, but they also contain amino acids conserved only among Pk1 or Pk2 (Fig. S5 B). Therefore, we tested whether these unique amino acids are responsible for the specific functional activities of Pk1 and Pk2.

The insertion of the Pk1 STR domain into the Pk2 backbone suppressed the tissue-fluidizing activity of Pk2 (Pk2(1STR) in Fig. 7, H and I–K), whereas the complementary construct had the opposite effect (Pk1(2STR) in Fig. 7, E and I–K). The rescue by the STR domain was less complete than the rescue by Pk2N-Pk1C or Pk1N-Pk2C. However, swapping the VBDs did not affect cell packing (Fig. S6, I–P). These results suggest that the STR domain is responsible for the tissue-fluidizing activity of Pk2, whereas it

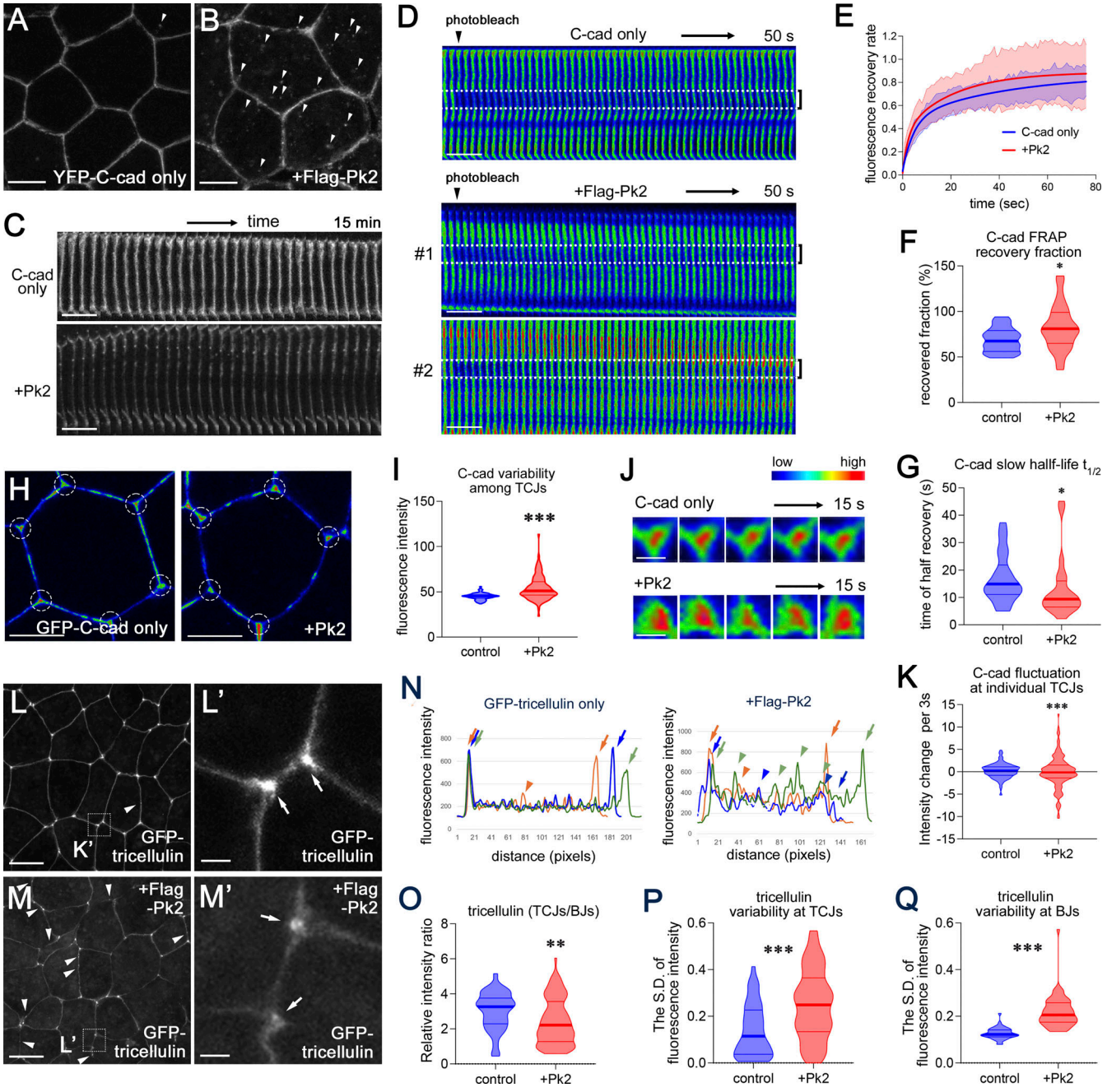


Figure 5. **Destabilization of AJs and TCJs in Pk2-overexpressing ectoderm. (A and B)** Representative images of YFP-C-cadherin in the control (A) or Pk2-overexpressing (B) ectoderm. Snapshots from Video 8 (durations of 14 min 30 s at 30-s time intervals). Arrowheads indicate C-cadherin puncta in the cytoplasm. Imaging was initiated at stage 11.5. **(C)** Representative kymographs of YFP-C-cadherin at BJs from Video 8. Single *z*-plane images. **(D)** Representative kymographs of GFP-C-cadherin FRAP experiments. Arrowheads indicate the timing of photobleaching. Brackets show the sites of photobleaching. The recovery of GFP-C-cadherin fluorescence signals was quantified in areas outlined by the white-dotted line. In Pk2 #1 junctions, the recovery of GFP-C-cadherin did not reach the prebleach level. In Pk2 #2 junctions, the recovery of GFP-C-cadherin exceeded the prebleach level. **(E)** Representative curve fitting of GFP-C-cadherin FRAP in the control (blue) and Pk2 OE (red) ectoderms. The light blue and red regions represent the S.D. values. GraphPad was used for curve fitting. **(F and G)** Percent GFP-C-cadherin recovery (F) and the halftime of recovery (G) in the control and Pk2 OE ectoderms. The percent recovery was based on calculated plateau values. AJs with unstable plateau values were excluded. 28 AJs (control) and 28 AJs (+Flag-Pk2) from more than five embryos were used. The Mann–Whitney U test was used to compare mean ranks. **(H)** Representative images of GFP-C-cadherin at TCJs in control and Pk2 OE cells. The white circles indicate TCJs. **(I)** Quantification of YFP-C-cadherin variability among TCJs. The integrated fluorescence intensity of YFP-C-cadherin at TCJs was quantified in still images. 186 TCJs (control) and 107 TCJs (+Flag-Pk2) from three embryos were used. **(J)** Representative snapshot images of GFP-C-cadherin fluctuations at single TCJs from time-lapse imaging in the control and Pk2 OE ectoderms. **(K)** Quantification of YFP-C-cadherin fluctuations at individual TCJs. Changes in YFP-C-cad intensity at individual TCJs were quantified after time-lapse imaging. 10 TCJs (control) and 10 TCJs (+Flag-Pk2) per embryo were used. Three embryos per group were used. The Kolmogorov–Smirnov test was used to compare distributions in I and K. **(L–M′)** Representative images of GFP-tricellulin in stage 11 control (L and L′) and Flag-Pk2 OE (M and M′) ectoderms. The square areas in L and M are enlarged in L′ and M′. The arrowheads indicate ectopic enrichment of GFP-tricellulin at BJs. The arrows indicate tricellulin accumulation at TCJs. **(N)** Line plots of GFP-tricellulin fluorescence intensity at three junctions. The pairs of

orange, blue, and green arrows indicate the TCJs. The arrowheads indicate mislocalization of tricellulin at the BJs. **(O)** Quantification of GFP-tricellulin accumulation at TCJs in the control and Pk2 OE ectoderms. The fluorescence intensity of GFP-tricellulin at individual TCJs was normalized to the average fluorescence intensity of GFP-tricellulin at BJs from the same images. **(P and Q)** Variations in GFP-tricellulin intensity at the TCJs (P) and BJs (Q) are shown as S.Ds. 83 TCJs (control) and 87 TCJs (Pk2 KD) from three embryos per group were used. The Mann–Whitney U test was used to compare mean ranks (O–Q). ***P < 0.001, **P < 0.01, *P < 0.05. Scale bars: 20 µm (A, B, L, and M), 5 µm (C and D), 10 µm (H), and 2 µm (J, L′, and M′).

may require additional domains for full activity. For further assessment, the STR swap mutants were mosaically expressed in the ectoderm. The STR of Pk1 was sufficient to change the shape of mosaic cells to more concave (Pk2(1STR) in Fig. S6 E). The complementary construct changed the cell shape to more convex (Pk1(2STR) in Fig. S6 D). We quantified cell shape changes by circularity and solidity (Fig. S6, F–H), the parameters for compactness and convexity of shapes, via particle measurement tools in ImageJ. A maximum value of 1 represents a perfect circle (Ant et al., 2023; Cox, 1927; Msibi and Mabandla, 2019; Zanier et al., 2015). The OE of Pk3, which does not contain STR (Fig. S5 A), did not inhibit hexagonal packing with or without Vangl2 coexpression (Fig. S5, D and F–I). These results suggest that the STR domain is responsible for the functional differences between Pk1 and Pk2 in AJ remodeling or actomyosin.

### Pk2 requires Rac1 to increase tissue fluidity in the gastrula ectoderm

Rho family small GTPases regulate AJs and actomyosin (Arnold et al., 2017; Citi et al., 2014; Heasman and Ridley, 2008). Our attempt to test the physical interaction of Pk2 with ARHGAP21/23 was not successful because of nonspecific binding. Alternatively, we coexpressed the dominant interfering forms of RhoA or Rac1 (DN-RhoA or DN-Rac1) (Hall, 1998) in the gastrula ectoderm to test the requirement of Rho or Rac1 for Pk2 ability to promote tissue fluidity.

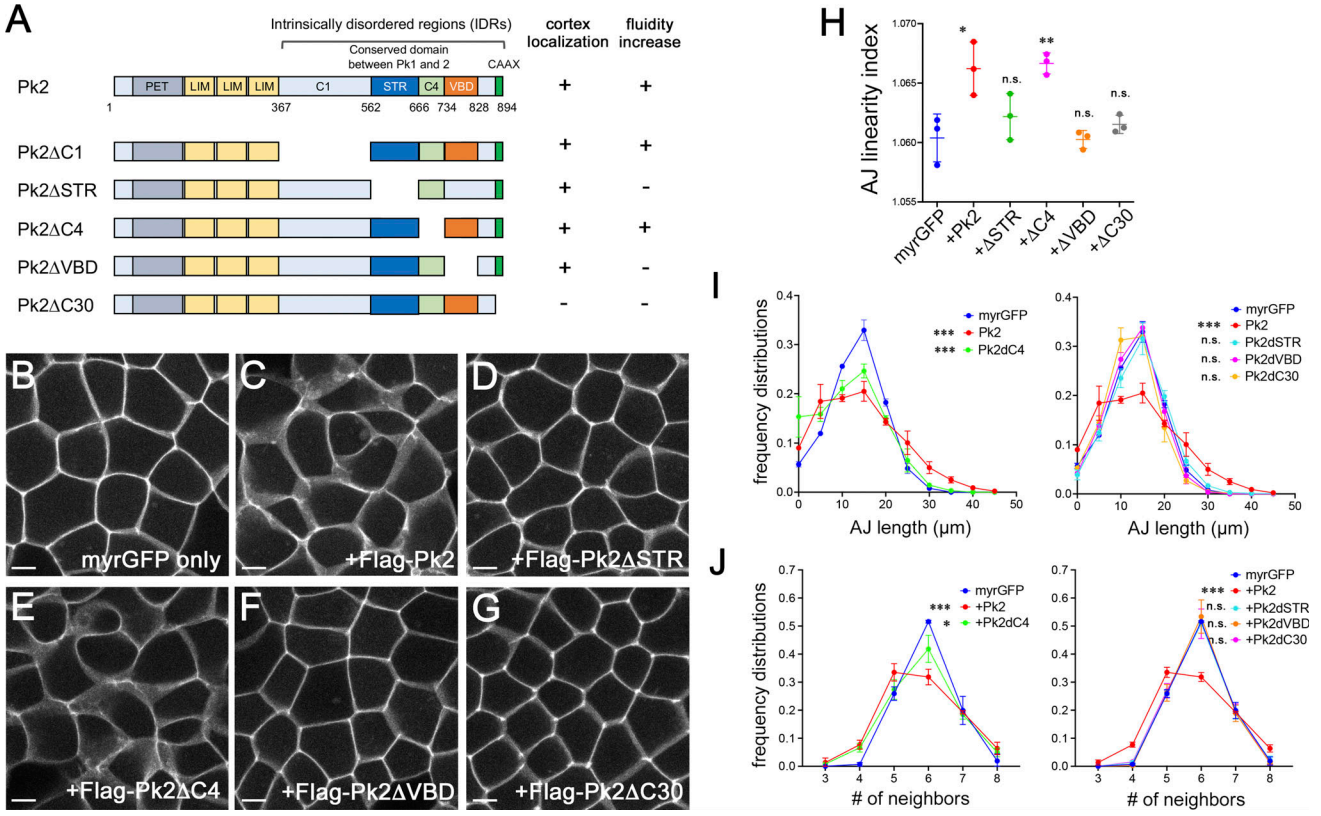


Figure 6. **STR is required for Pk2-mediated inhibition of cell packing. (A)** Scheme of Pk2 deletion mutant constructs. Pk2 contains one PET, three LIM domains, intrinsically disordered regions (IDRs), and a CAAX motif. The IDRs include three conserved regions: the STR, the VBD, and the C4 region between the STR and VBD. **(B–G)** Representative images of stage 11 ectoderms expressing myrGFP only (B) or myrGFP with Pk2 deletion mutants (C–G). Albino embryos were used to visualize the lateral domain. **(H–J)** Tissue fluidity was evaluated by scoring AJ linearity (H), AJ length distribution (I), and the number of neighboring cells (J). Pigmented wild-type embryos were used for quantification. AJ linearity was quantified as described in Fig. 3 H. Individual dots represent the average AJ linearity in one embryo, and lines represent the average linearity of three embryos in H. Original numerical data were used in H and I. One-way ANOVA was used to compare mean ranks, with the Bonferroni correction for multiple pairwise comparisons in H. The Kolmogorov–Smirnov test was used to compare distributions in I. The chi-square test was used in J. Three embryos per group were used. The total number of cells and AJs was as follows: 308 cells and 1,050 AJs (myrGFP); 517 cells and 1,722 AJs (+Pk2); 296 cells and 1,019 AJs (+Pk2ΔSTR); 396 cells and 1,366 AJs (+Pk2ΔC4); 334 cells and 1,151 AJs (+Pk2ΔVBD); 378 cells and 1,272 AJs (+Pk2ΔC30). *P < 0.05, **P < 0.01, ***P < 0.001, n.s., not significant. Scale bars: 10 µm.

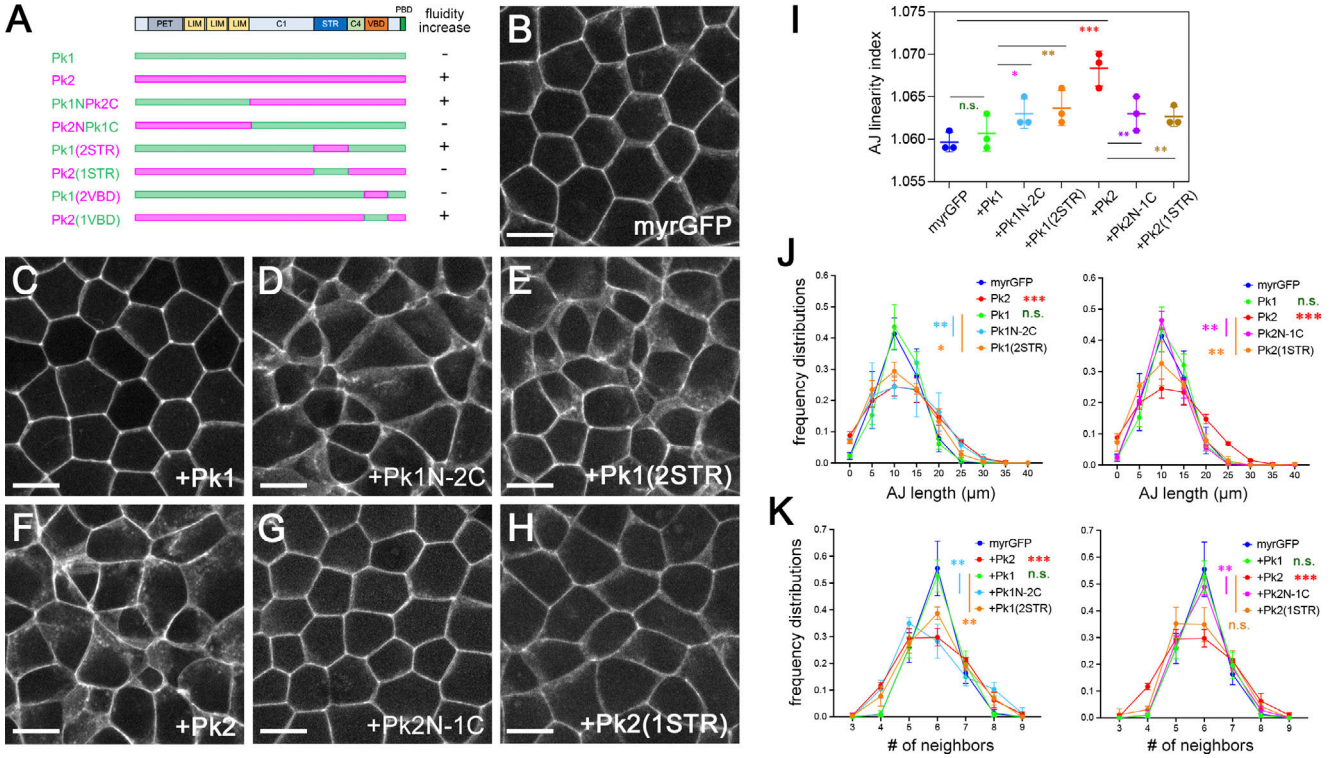


Figure 7. **STR is responsible for the inhibition of cell packing by Pk2. (A)** Schematic diagrams of the Pk1-Pk2 chimeric constructs. **(B–H)** Representative images of stage 11.5 ectoderms expressing myrGFP only (B), HA-Pk1 (C), Flag-Pk1NPk2C (D), HA-Pk1(2STR) (E), Flag-Pk2 (F), HA-Pk2NPk1C (G), and Flag-Pk2(1STR) (H). Albino embryos were used for imaging. Wild-type pigmented embryos were used for segmentation and quantification. **(I–K)** Cell packing was evaluated by scoring AJ linearity (I), AJ length distribution (J), and the number of neighboring cells (K). Three embryos per group were used. Original numerical data were used for statistical analyses in I and J. One-way ANOVA was used to compare the mean ranks, with the Bonferroni correction for multiple pairwise comparisons in I. The two-sample Kolmogorov–Smirnov test was used to compare distributions in J. The chi-square test was used in K. The total number of cells and AJs was as follows: 284 cells and 966 AJs (myrGFP only); 221 cells and 783 AJs (+Pk1); 189 cells and 646 AJs (+Pk1N-Pk2C); 253 cells and 761 AJs (+Pk1(2STR)); 206 cells and 702 AJs (+Pk2); 186 cells and 596 AJs (+Pk2N-Pk1C); 169 cells and 1,228 AJs (+Pk2(1STR)). *P < 0.05, **P < 0.01, ***P < 0.001, n.s., not significant. Scale bars: 20 μm.

DN-Rac1 suppressed, while DN-RhoA somewhat enhanced, the effects of Pk2 OE on cell packing (Fig. 8, D–G, J, and K). The complementary effects of DN-Rac1 and DN-RhoA on Pk2 activity are consistent with the mutually antagonistic roles of RhoA and Rac1 in actomyosin and AJs (Burridge and Wennerberg, 2004; Chauhan et al., 2011). Neither DN-RhoA nor DN-Rac1 had a substantial effect on their own (Fig. 8, B, C, and G–I). Taken together, these results suggest that Pk2 requires active Rac1 to promote AJ remodeling.

### Pk2 promotes neuroepithelial cell elongation in the AP direction

Pk2 KD attenuated AJ remodeling and reduced the orientation-based patterns of AJ behaviors in the NE (Fig. 2 H; and Fig. S1, K and L). Pk2 OE in the ectoderm promoted AJ remodeling, but the direction of AJ remodeling was random (Fig. S3 E), suggesting that factors other than Pk2 control the direction of AJ remodeling in the NE. To test this hypothesis, we expressed Pk2 in the NE at relatively high levels, leading to its uniform distribution at AJs (high Pk2 in Fig. 9 A). Compared with the control, uniform Pk2 OE in the NE increased the fraction of cells that extended along the AP axis (Fig. 9, B, C, and F; and Video 10). Although Pk1 OE did not have this activity (Fig. 9, D and G; and Video 10), Pk1(2STR) did (Fig. 9, E and H; and Video 10), further supporting the role of the STR domain of Pk2 in junction remodeling. These findings suggest that Pk2 has a permissive rather than instructive role in anisotropic AJ remodeling in the NE and requires another factor(s) for the directionality of the response.

Moderately expressed exogenous Pk2 preferentially localizes at anterior AJs in the NE (low Pk2 in Fig. 10 A) (Butler and Wallingford, 2018). When the increase in Pk2 was limited to anterior AJs, Pk2 OE did not elongate NE cells along the AP axis (compare Fig. 9 A and Fig. 10 A) or disrupt NTC (Fig. 10 B). However, tracking of individual AJs revealed that Pk2(low) further enhanced the anisotropy of AJ remodeling in the NE, as confirmed in three independent embryos (Fig. 10 C). The overall rate of AJ elongation increased (Fig. 10 D), whereas AJ shrinkage was not significantly affected (Fig. 10 E). Thus, while the Pk2 protein itself does not have an instructive role, its planar localization at anterior AJs enhances the anisotropy of AJ remodeling in the NE, cooperating with instructive cues in the environment.

## Discussion

This study reveals a previously uncharacterized role of Pk2 in tissue fluidity in the *Xenopus* ectoderm during neurulation.

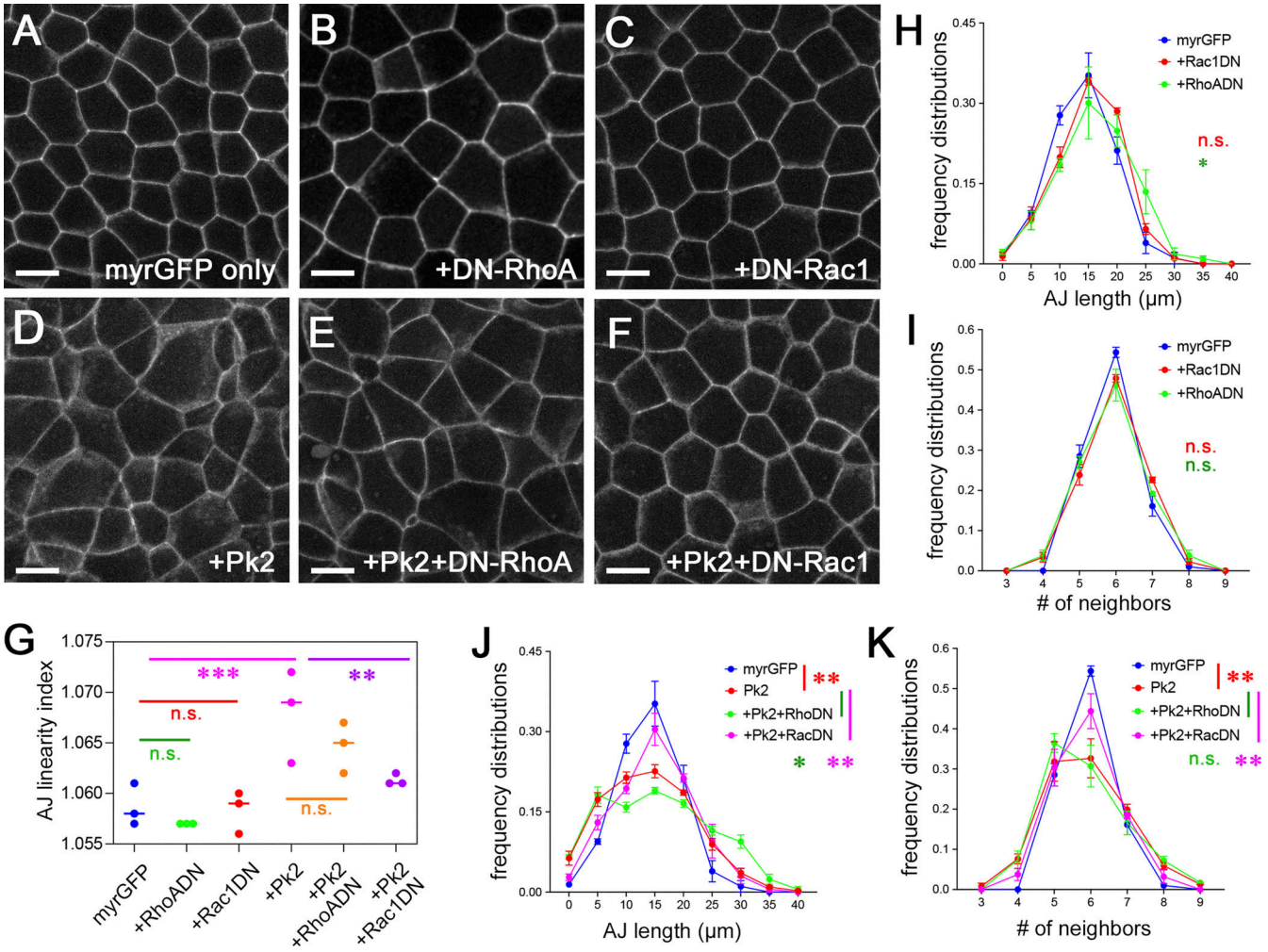


Figure 8. **Rac1 activation is required for the inhibition of cell packing by Pk2. (A–F)** Representative images of *Xenopus* gastrula ectoderms expressing myrGFP only (A), myrGFP with DN-RhoA (B), DN-Rac1 (C), Flag-Pk2 (D), Flag-Pk2+DN-RhoA (E), or Flag-Pk2+DN-Rac1 (F). Imaging was initiated at stage 11.5. Pigmented wild-type embryos were used for image acquisition and quantification. **(G–K)** Quantification of cell packing on the basis of variations in AJ linearity (G), AJ length (H and J), and the number of neighboring cells (I and K). Statistical analyses in G, H, and J were conducted on the original numerical data. One-way ANOVA was used to compare mean ranks, with the Bonferroni correction for multiple pairwise comparisons in G. The Kolmogorov–Smirnov test was used to compare distributions in H and J. The chi-square test was used in I and K. Three embryos per group were used. The total number of cells and AJs was as follows: 214 cells and 781 AJs (myrGFP only); 161 cells and 594 AJs (DN-RhoA only); 184 cells and 681 AJs (DN-Rac1 only); 236 cells and 828 AJs (Pk2 only); 177 cells and 656 AJs (Pk2 with DN-RhoA); and 189 cells and 694 AJs (Pk2 with DN-Rac1). *P < 0.05, **P < 0.01, ***P < 0.001, n.s., not significant. Scale bars: 20 μm.

Loss-of-function and gain-of-function approaches have shown that Pk2 is required to maintain the fluidity of AJs and enhance the anisotropy of AJ remodeling in the NE, a tissue with high fluidity. In contrast, Pk2 OE helped us assess its inhibitory effects on cell packing in nonneural ectoderm, a tissue with low fluidity, and test the requirement of the STR domain in controlling tissue fluidity. In our model, Pk2 promoted AJ remodeling (Fig. 10 F), stimulating cell shape changes and cell–cell rearrangements in the epithelia (Fig. 10 G). Vangl2 association is required for the full activity of Pk2. Given the anterior enrichment of Pk2 and Vangl2 in the NE (Fig. 10 A) (Butler and Wallingford, 2018; Ossipova et al., 2015c), Pk2 may locally increase junction remodeling at anterior BJs and TCJs, where the crescent-shaped actomyosin network promotes the elongation of AP junctions (Fig. S2). We propose that environmental chemical or mechanical cues cooperate with Pk2 to direct anisotropic AJ remodeling and tissue deformation. The anterior localization of Pk2 in the NE amplifies the effect of anteroposteriorly oriented environmental cues on AJ remodeling (Fig. 10 H). These cues may include tensile stresses originating from the elongation of the embryo body axis (Christodoulou and Skourides, 2022; Clausi and Brodland, 1993; Davidson and Keller, 1999; Handler et al., 2023; Hirano et al., 2022; Moon and Xiong, 2022; Smith and Schoenwolf, 1997; Sokol, 2016; Xiong et al., 2020; Zhou et al., 2015). Alternatively, diffusible morphogen gradients may be responsible for the directionality of Pk2 effects. In support of the latter possibility, several Wnt and FGF ligands are expressed predominantly posteriorly, in a graded manner during neurulation (Aulehla and Pourquié, 2010; Diez Del Corral and Morales, 2017; Edri et al., 2023; Niederreither et al., 1999; Nordström et al., 2002; Storey et al., 1998; Yamaguchi, 2001; Yoon et al., 2023).

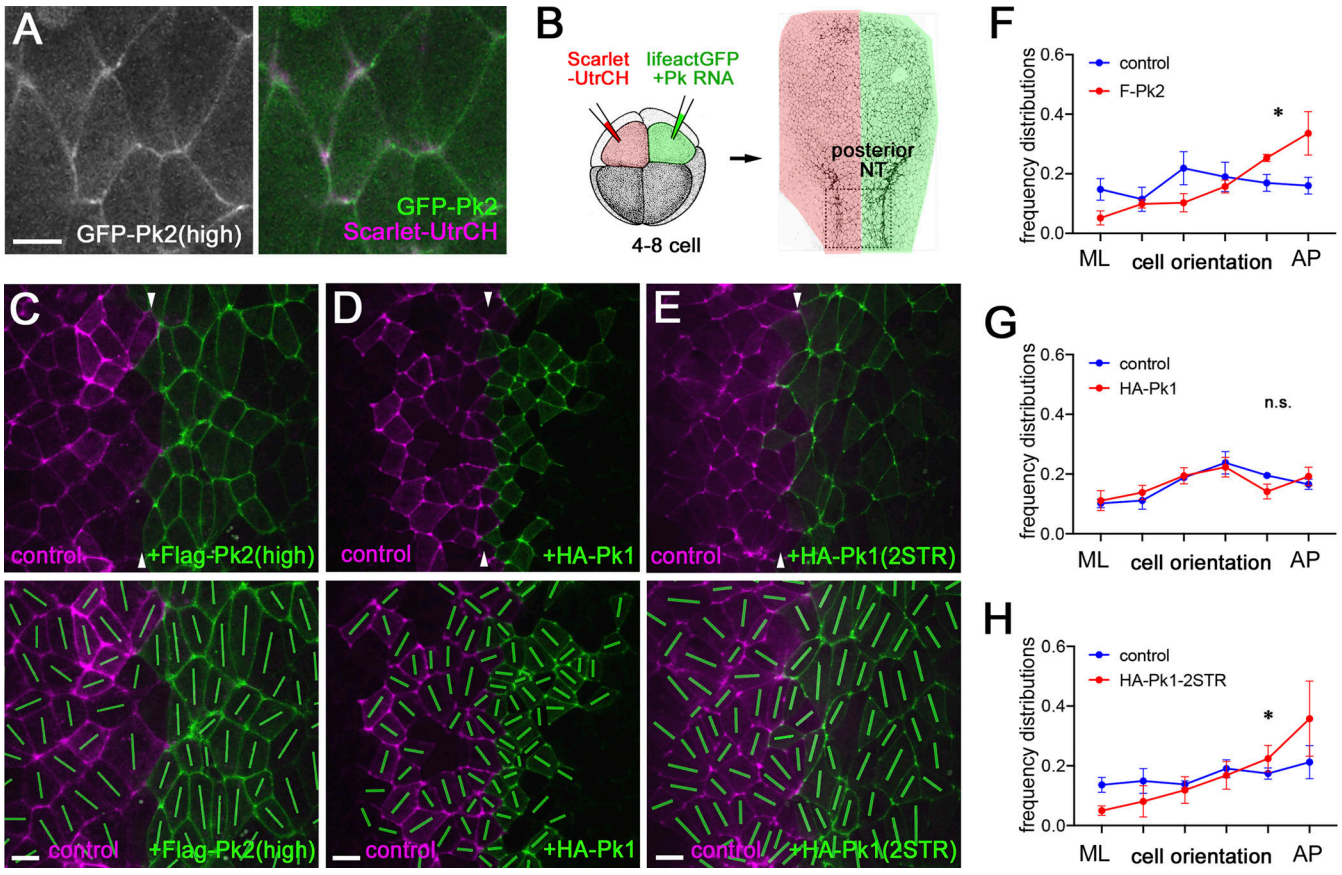


Figure 9. **Uniform Pk2 promotes AP elongation in NE cells. (A)** GFP-Pk2 distribution (high) in stage 15–16 NEs with Scarlet-UtrCH as an AJ marker. **(B)** Scheme of the experiments for Fig. 9 and Fig. 10. Lifeact-GFP RNA was coinjected with HA-Pk1, Flag-Pk2, or HA-Pk1 (2STR) RNA into one dorsal-animal blastomere (green) at the four- to eight-cell stage. Scarlet-UtrCH RNA was injected into the other dorsal-animal blastomere (red) as a control. The posterior NE close to the border between the brain and the spinal cord was imaged. **(C–E)** Representative images of NEs expressing Lifeact-GFP with Flag-Pk2 (C), HA-Pk1 (D), or HA-Pk1(2STR) (E) from Video 10. Arrowheads indicate the presumable midline of the embryos. **(F–H)** Frequency distribution histogram of cell orientation in the NE. The control and Pk-OE sides of the NE were compared in the same time-lapse imaging field. Average and ±S.D. are shown. The Kolmogorov–Smirnov test was conducted to compare distributions, using original numerical data. Four embryos per group were used. The total number of cells was as follows: *n* = 403 (control) and 562 (Flag-Pk2 (high)) (G); *n* = 367 (control) and 350 (HA-Pk1) (H); and *n* = 484 (control) and 528 (HA-Pk1 (2STR)). Scale bars: 20 µm. *P < 0.05. n.s., not significant.

Mechanistically, the Pk2 STR domain and Rac1 activity play key roles in Pk2-stimulated AJ remodeling. The presence of the STR domain in Pk1 and Pk2 parallels their ability to affect cell morphology (Carreira-Barbosa et al., 2003; Huang and Winklbauer, 2022; Tao et al., 2009; Veeman et al., 2003; Zhang et al., 2016). Rac1 is a well-known regulator of AJ remodeling (McCormack et al., 2013; Nelson, 2009; Watanabe et al., 2009) that can directly affect AJ components or via the reorganization of the actomyosin network (Chen et al., 2017; Daneshjou et al., 2015; Erasmus et al., 2015; Grikscheit et al., 2015; Izumi et al., 2004; Timmerman et al., 2015). Increased actomyosin dynamics in Pk2-overexpressing tissue supports the latter possibility. Pk2 KD may reduce actomyosin contractility at T1 junctions to attenuate AJ elongation as reported during tissue elongation in *Drosophila* embryos (Collinet et al., 2015; Finegan et al., 2019; Uechi and Kuranaga, 2019; Yu and Fernandez-Gonzalez, 2016). Alternatively, Pk2 may increase cadherin turnover through Rab11-mediated endocytic and recycling machinery (Akhtar and Hotchin, 2001; Amin et al., 2013; Bouchet et al., 2016; Erasmus et al., 2021; Frasa et al., 2010; Wayt et al., 2021; Woichansky et al., 2016). In our model, Pk2 binds RhoA-GAPs via its STR domain and locally activates Rac1, similar to ARHGAP21/23 binding to the STR domain of Pk1 (Zhang et al., 2016). Considering the functional differences between Pk1 and Pk2, the STR domain of Pk2 may interact with Rac1 regulators other than ARHGAP21/23. Identification of these GAPs or GEFs will be necessary to further characterize the function of the Pk2-Rac1 pathway in junction remodeling and actomyosin reorganization.

The role of Vangl2, a known binding partner of Pk2, in tissue fluidity remains unclear. Vangl2 OE did not affect cell packing in the gastrula ectoderm (Fig. S5, E and G–I) or cell reorientation in the NE (Matsuda et al., 2023), but its binding to Pk2 appears to be required for full Pk2 activity in AJ remodeling. Due to the proximity of the VBD to the STR, Vangl2 association may regulate Pk2 interaction with Rho-GAPs or Rac-GEFs. Vangl2 has also been reported to bind N-cadherin and promote its internalization at synapses (Nagaoka et al., 2014), indicating that Vangl2 may link Pk2 to the control of cadherin dynamics. Another candidate is Par3, which binds Pk3 and controls NTC in *Xenopus*

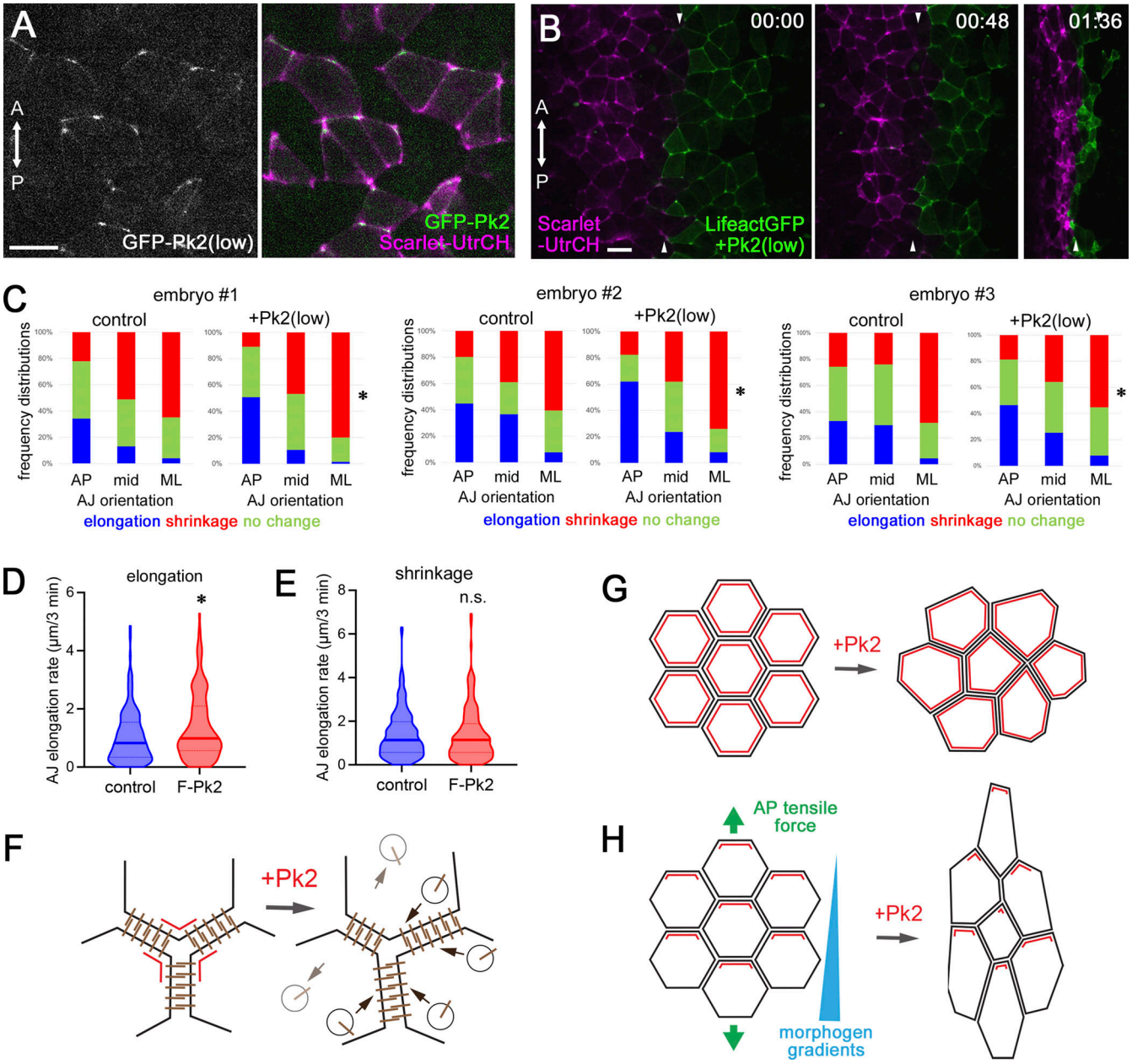


Figure 10. **Increased Pk2 at anterior AJs enhances anisotropic AJ remodeling in the NE. (A)** Distribution of GFP-Pk2 (low dose, 50 pg RNA) in the NE. Scarlet-UtrCH marks AJs. **(B)** Snapshot images of NEs expressing Scarlet-UtrCH only (purple, left) or Flag-Pk2 (low) with Lifeact-GFP (green right) from time-lapse imaging. Scale bars: 20 μm. **(C)** Quantification of changes in AJ length. The control and Pk2(low) sides of NEs were compared in the same embryos. Changes in AJ length were categorized as follows: elongation (blue, ≥0.8 μm/3 min), shrinkage (red, less than or equal to −0.8 μm/3 min), or no change (green, −0.8< and <0.8 μm/3 min). AJs were categorized into AP (≤30° from the AP axis), ML (≤30° from the ML axis), and mid (30–45° from either the AP or ML axes). The distributions of AJ length changes in AP and ML junctions were compared between the control and +Pk2(low) NE groups. The Kolmogorov–Smirnov test was used on original numerical data. Three embryos per group were used. The total counts in the plots were as follows: $n$ = 291 (control #1); $n$ = 280 (Pk2 (low) #1); $n$ = 253 (control #2); $n$ = 183 (Flag-Pk2 #2); $n$ = 360 (control #3); $n$ = 363 (Pk2 (low) #3). **(D and E)** Rates of AJ elongation (D) and shrinkage (E) in the control and Pk2(low) OE NEs. The same dataset used in C was used for this analysis. The bold and thin lines indicate medians and quartiles, respectively. The Mann–Whitney U test was used to compare mean ranks. *P < 0.05. n.s., not significant. **(F–H)** Models of Pk2-mediated tissue fluidity control. Pk2 (red) increases cadherin turnover by modulating the components of AJ complexes or increasing actomyosin dynamics at AJs, promoting AJ remodeling (F). In the absence of directional cues, Pk2-mediated AJ remodeling is directionally random (G). In the presence of directional cues, Pk2 locally increases the susceptibility of AJs to stimulus-induced remodeling (H).

embryos (Chuykin et al., 2018). Par3 is an essential regulator of apical–basal polarity and has been implicated in PCP signaling, actomyosin, and epithelial folding (Bellaïche et al., 2001; Besson et al., 2015; David et al., 2013; Ishiuchi and Takeichi, 2011; Sawyer et al., 2011; Simoes et al., 2010; Wang et al., 2012). Further studies of Vangl2, other PCP components, and their cellular targets are needed to elucidate how Pk2 controls directional AJ remodeling in response to embryonic cues.

## Materials and methods

### Plasmid, MO, and RNA preparation

pCS107-GFP-xPk2 was kindly provided by John Wallingford (University of Texas, Austin, TX, USA) (Butler and Wallingford, 2015, 2018). *Xenopus* Pk1S cDNA was obtained from Open BioSystems (Horizon). pCS2-3xFlag-xPk3 was generated from pCS2-Flag-Pk3 (Ossipova et al., 2015a) via PCR with primers containing the corrected C-terminal sequence (Pk3-F; 5′-GAG CTTAAGCGACCCAGATG-3′; Pk3-R: 5′-CTCGAGTTATGAAAG AAGGCAACTTTTG-3′). Subcloned Pk2 deletion mutants or Pk1S was inserted into either pCS107-Flag or pCS2-3xHA via restriction enzymes and T4 ligase. The domains in the C-terminal half of Pk2 are defined as follows: C1 (aa. 367–561), STR (aa. 562–665), C4 (aa. 666–733), and VBD (aa. 734–827). The NEBuilder HiFi DNA Assembly Mastermix (catalog # E2621; NEB) was used for the construction of chimeric Pk1 and Pk2 mutants using the following primers: FLAG-PK2-N-V-R: 5′-TTCTCCCACACTGCA TGC-3′; FLAG-PK2-N-V-F: 5′-TCCTAGGCGGCCGCGGC-3′; PK1S-C-I-F: 5′-GCATGCAGTGTGGGAGAAGATGTGCATGCATCG-3′; PK1S-C-I-R: 5′-GCCGCGGCCGCCTAGGAAATAATGCAGTTTTTG CC-3′; HA-PK1S-V-F: 5′-GATGTGCATGCATCGGAC-3′; HA-PK1S-V-R: 5′-TGAATTCGCGTAATCTGG-3′; PK2-N-I-F: 5′-CCAGAT TACGCGAATTCAATGTTTAACCGGAGC-3′; PK2-N-I-R: 5′-GTC CGATGCATGCACATCTTCTCCCACACTGCATG-3′; PK1S-C1-V-R: 5′-TTCTTGTAGCTTTCGGC-3′; PK1S-C4-V-F: 5′-GAATTAACT GCACAGAATAATATCCGTCGGCCGC-3′; PK2-C2-I-F: 5′-GCAGCC GAAAGCTACAAGAAAAGTTTGAGGAAAAGAAGC-3′; PK2-C2-I-R: 5′-ATTATTCTGTGCAGTTAATTC-3′; PK2-C1-V-R: 5′-GGGAAC TCTGAGACTGG-3′; PK2-C4-V-F: 5′-GGAGACTACAGCAGCATA GAAATAAAAATGACCCCGATG-3′; PK1S-C2-I-F: 5′-GATCCAGTC TCAGAGTTCCCCTGGATATGGATCACGG-3′; PK1S-C2-I-R: 5′-TTCTATGCTGCTGTAGTCTCC-3′. pCS2-GFP, myrGFP, and myrRFP were described previously (Matsuda et al., 2023). pCS2-3xGFP-mZO1 was subcloned from pCAGGS-GFP-mZO1 (Matsuda et al., 2004) by restriction enzyme and T4 ligase. pCS2-Lifeact-GFP was constructed from pCS2-GFP and annealed oligonucleotides encoding Lifeact probe peptides (Lifeact-F: 5′-CGATACCATGGG CGTGGCCGACTTGATCAAGAAGTTCGAGTCCATCTCCAAGGA GGAGAT-3′; Lifeact-R: 5′-CGATCTCCTCCTTGGAGATGGACTCGA ACTTCTTGATCAAGTCGGCCACGCCCATGGTAT-3′). Scarlet-UtrCH was inserted into the pCS2 vector from 3xmScarlet I-UtrCH, a gift from Dorus Gadella (University of Amsterdam, Amsterdam, Netherlands) (plasmid # 112962; Addgene) (Chertkova et al., 2020, *Preprint*) using restriction enzyme and T4 ligase. pT7T-C-cadherin-mYFP and pT7T-C-cadherin-GFP were generated from pT7T-CcadTSMod, a gift from Marc Tramier (University of Rennes, Rennes, France) (plasmid # 99874; Addgene) (Herbomel et al., 2017), by swapping TSMod to either mYFP or GFP. pCS2-mNeonGreen-Sf9 and pCS2-GFP-tricellulin were generous gifts from Ann Miller (University of Michigan, Ann Arbor, MI, USA) (Higashi et al., 2016) and Ed Munro (University of Chicago, Chicago, IL, USA). Sf9 is a single-chain variable fragment (scFv) of an antibody to NMII and is used as a biosensor of NMIIA (Hashimoto et al., 2015). DN-RhoA and DN-Rac1 in the pRK5 vector were gifts from Alan Hall (Sloan-Kettering Institute, New York, NY, USA) (Hall, 1998). Capped RNA was synthesized via mMESSAGE mMACHINE SP6 Transcription Kit (catalog # AM1340; Thermo Fisher Scientific) and purified with RNeasy Mini Kit (catalog # 74104; Qiagen). *Pk2* MO (5′-GAACCCAAACAA ACACTTACCTGTT-3′) and *Pk1* MO (5′-CTTCTGATCCATTTCCAA AGGCATG-3′) (Gene Tools) were characterized in previous studies (Butler and Wallingford, 2018; Daulat et al., 2012; Huang and Winklbauer, 2022; Takeuchi et al., 2003).

### *Xenopus* embryos and microinjection

Wild-type and albino *Xenopus laevis* were purchased from Nasco and Xenopus1, and maintained and handled following the Guide for the Care and Use of Laboratory Animals of the National Institutes of Health. The protocol for animal use was approved by the Institutional Animal Care and Use Committee (IACUC) of the Icahn School of Medicine at Mount Sinai. The sex of the animals was not considered in the study design or analysis because the study subjects were sexually indifferent embryos. In vitro fertilization and embryo culture were performed as previously described (Ossipova et al., 2014). Embryo staging was determined according to Nieuwkoop and Faber (Nieuwkoop and Faber, 1994). For microinjections, embryos were transferred to 3% Ficoll PM400 (catalog # 170300; Cytivia) in 0.5× Marc's modified Ringer's (MMR) solution (50 mM NaCl, 1 mM KCl, 1 mM $CaCl_2$, 0.5 mM $MgCl_2$, and 2.5 mM HEPES [pH 7.4]) (Peng, 1991).

RNA or MO in 5–10 nl of RNase-free water (catalog # AM9937; Thermo Fisher Scientific) was microinjected into one to two animal blastomeres of four- to eight-cell-stage embryos. For apical domain imaging of gastrula embryos, two ventral-animal blastomeres were injected with 150 pg of RNA encoding Flag- or HA-tagged Pk proteins and coinjected with tracer RNA, including 50 pg of myrGFP, 50 pg of Lifeact-GFP, 50 pg of Scarlet-UtrCH, 200 pg of mNeonGreen-Sf9, 20 pg of tricellulin-GFP, or 100 pg of 3xGFP-ZO1. For apical domain imaging of the neurula, one dorsal-animal blastomere was injected with either 10 ng of Pk2 MO, 150 pg of Flag-Pk2 or HA-Pk1 RNA for high expression, or 50 pg of Flag-Pk2 for low expression, together with 50 pg of myrGFP or 50 pg of Lifeact-GFP. The other dorsal-animal blastomere was injected with 50 pg of myrRFP or 50 pg of Scarlet-UtrCH. For imaging of actomyosin in the NE, 200 pg of mNeonGreen-Sf9 RNA and 50 pg of Scarlet-UtrCH RNA were coinjected with or without 10 ng of Pk2 MO into one dorsal-animal blastomere of a four- to eight-cell-stage embryo. For imaging to determine Pk2 distribution, RNA encoding GFP-Pk2 or Pk2 deletion mutants was coinjected with 50 pg RNA encoding myrRFP or Scarlet-UtrCH. RNA- or MO-injected embryos were cultured in 0.1x MMR until the early gastrula or neurula stage. Each injection included at least 20 embryos per condition. The experiments were repeated at least three times.

### Phalloidin staining and imaging of fixed *Xenopus* embryos

For phalloidin staining of the neurula, embryos were fixed in MEMFA (100 mM MOPS [pH 7.4], 2 mM EGTA, 1 mM $MgSO_4$, 3.7% formaldehyde) (Harland, 1991) for 1 h at room temperature. After permeabilization in 0.1% Triton X-100 in PBS for 10 min, the embryos were incubated with Alexa Fluor 555–conjugated phalloidin (1:400 dilution; catalog # A34055; Thermo Fisher Scientific) in PBS containing 1% BSA overnight at 4°C. The dissected neural plate was mounted on a glass slide with two

coverglass spacers (0.13–0.17 mm) to minimize damage to the morphology of the NE.

Images of the fixed embryos were captured either by the BC43 spinning disk confocal microscope (Fusion Ver 2; Andor, Oxford Instruments) or by Zeiss LSM 980 with an Airyscan 2 confocal microscope (Zen [blue edition] Ver 3.7.97.04000, Zeiss). Nikon CFI Plan Apochromat Lambda D 20× (NA = 0.8 and WD = 0.8 mm), Nikon CFI Plan Apo Lambda S 40XC Sil (NA = 1.25 and WD = 0.3 mm), Zeiss Plan Apochromat 20×/0.8 (NA = 0.8 and WD = 0.55 mm), or Zeiss C-Apochromat 40×/1.2 W (NA = 1.2 and WD = 0.28 mm) were used for gastrula imaging. Nikon CFI Plan Apochromat Lambda D 20× (NA = 0.8 and WD = 0.8 mm) was used for imaging the neurula. The experiments were repeated at least three times. Each experiment included at least three embryos per experimental group. Z-stack images were projected into a single image via the maximum projection function in ImageJ2 (ver. 2.9.0/1.54 g), which was used for further analysis and quantification.

### Time-lapse imaging of *Xenopus* embryos

Embryos were injected with RNA encoding Pks and fluorescent protein-tagged marker proteins. 5 to 10 embryos per individual group were mounted in 1% low melting temperature agarose (catalog # 50101; Lonza) in 0.1× MMR on a glass slide attached to a silicone isolator (1.6 mm depth; catalog # 664204; Grace Biolabs) or on a glass-bottom dish (catalog # D35-28-1.5-N; Cellvis). Time-lapse imaging was carried out at room temperature either on an Andor BC43 spinning disk confocal microscope, a Zeiss LSM 980 confocal microscope, or a Zeiss Axio Zoom V16 fluorescence stereomicroscope equipped with an AxioCam 506 mono CCD camera. Images were taken every 1 s to 6 min for a period of 15 min to 5 h. The multiposition tool in Fusion or Zen (blue edition) imaging software was used for simultaneous time-lapse imaging. Z-stack images were projected into a single image via the maximum projection function in ImageJ.

### FRAP analysis

FRAP was performed on stage 11–11.5 embryos via a Zeiss LSM 980 confocal microscope with Zeiss C-Apochromat 40×/1.2 W (NA = 1.2 and WD = 0.28 mm) at room temperature. A circular region 2 µm in diameter in the animal-side ectoderm was photobleached via a 488-nm laser (20% laser power; 1.02-µs/pixel dwell time, 10 iterations). The embryos were imaged every second after photobleaching for 80 s. GraphPad Prism (ver.10.3.1) was used to fit the C-cadherin FRAP data with a two-phase exponential curve and determine the halftime of recovery and the recovered fractions of cadherins. Statistical significance was determined by unpaired Student's *t* test.

### Data analysis, segmentation, cell tracking, and apical domain assessment

Image processing and quantification were performed as previously described (Matsuda et al., 2023). Briefly, grayscale images of the cell outline marker were segmented via the Python package CellPose v2.0.5 (Pachitariu and Stringer, 2022). Segmented cells were tracked across time points via the Python package Bayesian Tracker (btrack v0.4.5) (Ulicna et al., 2021) with manual correction. For NP segmentation, the NP area was defined by brighter signals of either Lifeact-GFP, Scarlet-UtrCH, or phalloidin staining than in the surrounding epidermis. Pigmented wild-type embryos were used for image segmentation.

### Analysis of junction morphology and fluorescence intensities

The morphology and fluorescence intensity of individual junctions and apical domains were quantified as described previously (Matsuda et al., 2023). Briefly, after segmentation, each TCJ was first identified as a vertex or edge of the cell outline network. Each BJ was identified between two vertices. The mean fluorescence intensities were measured via dilated masks of the pixel or a set of pixels that defined BJs and TCJs (five pixels, 0.76155 µm in width or diameter). The medioapical domain was the area that did not correspond to TCJs or BJs.

### Statistics and reproducibility

Histograms and dot plots of the experimental data were generated via GraphPad Prism 10 (ver. 10.1.0) and Microsoft Excel. Individual experiments were repeated at least three times. The standard deviations (S.Ds.) were calculated via GraphPad Prism 10 and used to assess the variability among sample groups. Student's *t* test (two-sided) or the Mann–Whitney test was used to compare means or mean ranks between two groups, respectively. One-way ANOVA was used to compare the means of more than two groups, with the Bonferroni correction for pairwise comparisons. The two-sample Kolmogorov–Smirnov test was used to compare distributions between two groups. The chi-square test was used for the categorical data.

### Online supplemental material

Fig. S1 shows Pk2 KD inhibits AP cell orientation in the NE. Fig. S2 shows asymmetrical actomyosin network formation during T1 transition and AJ elongation. Fig. S3 shows Pk2 promotes the elongation of newly formed AJs after cytokinesis. Fig. S4 shows Pk2 changes the organization of the actomyosin network at TCJs. Fig. S5 shows neither Pk1 nor Pk3 increases tissue fluidity in the gastrula ectoderm. Fig. S6 shows the STR is responsible for the functional difference between Pk1 and Pk2 on AJs and actomyosin. Video 1 shows a representative time-lapse video showing the dynamics of NE cells during NTC in Pk2-KD embryos. Video 2 shows a representative time-lapse video of the control (left) and Pk2-depleted NEs (right). Video 3 shows a representative time-lapse video showing changes in cell orientation (green lines) in control NEs and Pk2-KD NEs. Video 4 shows a representative time-lapse video of the Pk1 morphant NE. Pk1 MO was coinjected with Lifeact-GFP in one dorsal blastomere. Video 5 shows a representative time-lapse video of the NE expressing Scarlet-UtrCH and sf9-mNeon, which are live probes for F-actin and NMII. Video 6 shows a representative time-lapse video showing hexagonal packing during gastrulation in wild-type (left) and Flag-Pk2 OE (right) embryos. Video 7 shows a representative time-lapse video showing hexagonal packing and lateral domain dynamics in the control wild-type (left) and Flag-Pk2 OE (right) ectoderms. Video 8 shows a representative time-lapse video showing YFP-C-cadherin dynamics in the control wild-type (left) and Flag-Pk2 OE (right) ectoderms. Video 9

shows a representative time-lapse video showing the dynamics of F-actin and NMII at TCJs. Video 10 shows a representative time-lapse video showing the dynamics of NE cells expressing high levels of Flag-Pk2 (left panel), HA-Pk1 (middle panel), or HA-Pk1(2STR) (right panel).

### Data availability

Data are available in the article itself and its supplementary materials. The imaging data that are not shown but used in the reported quantifications are available upon reasonable request from M. Matsuda or S.Y. Sokol.

## Acknowledgments

We thank D. Gadella, A. Hall, A. Miller, E. Munro, M. Tramier, and J. Wallingford for plasmids. We also thank Jakub Harnos and Chih-Wen Chu for the construction of plasmids encoding Pk2 deletion mutants. We are grateful to Tanya Whitfield, Karen Kasza, and Sassan Ostwar for their comments on the manuscript and members of the Sokol laboratory for valuable discussions. We acknowledge the help from the ISMMS Microscopy Core facility.

This research was supported by the National Institutes of Health grant R35GM122492 to S.Y. Sokol.

Author contributions: M. Matsuda: conceptualization, data curation, formal analysis, investigation, methodology, validation, visualization, and writing—original draft, review, and editing. S.Y. Sokol: conceptualization, funding acquisition, methodology, project administration, resources, supervision, and writing—original draft, review, and editing.

Disclosures: The authors declare no competing interests exist.

Submitted: 2 July 2024
Revised: 29 December 2024
Accepted: 21 January 2025

## References

Akhtar, N., and N.A. Hotchin. 2001. RAC1 regulates adherens junctions through endocytosis of E-cadherin. *Mol. Biol. Cell.* 12:847–862. https://doi.org/10.1091/mbc.12.4.847

Amin, E., B.N. Dubey, S.C. Zhang, L. Gremer, R. Dvorsky, J.M. Moll, M.S. Taha, L. Nagel-Steger, R.P. Piekorz, A.V. Somlyo, and M.R. Ahmadian. 2013. Rho-kinase: Regulation, (dys)function, and inhibition. *Biol. Chem.* 394:1399–1410. https://doi.org/10.1515/hsz-2013-0181

Ant, L., F.L. Dily, M. Beato, and P. Saragüeta. 2023. Quantitative analysis of cellular morphology during in vitro decidualization. *Curr. Protoc.* 3: e895. https://doi.org/10.1002/cpz1.895

Arnold, T.R., R.E. Stephenson, and A.L. Miller. 2017. Rho GTPases and actomyosin: Partners in regulating epithelial cell-cell junction structure and function. *Exp. Cell Res.* 358:20–30. https://doi.org/10.1016/j.yexcr.2017.03.053

Atia, L., J.J. Fredberg, N.S. Gov, and A.F. Pegoraro. 2021. Are cell jamming and unjamming essential in tissue development? *Cells Dev.* 168:203727. https://doi.org/10.1016/j.cdev.2021.203727

Aulehla, A., and O. Pourquié. 2010. Signaling gradients during paraxial mesoderm development. *Cold Spring Harb. Perspect. Biol.* 2:a000869. https://doi.org/10.1101/cshperspect.a000869

Aw, W.Y., and D. Devenport. 2017. Planar cell polarity: Global inputs establishing cellular asymmetry. *Curr. Opin. Cell Biol.* 44:110–116. https://doi.org/10.1016/j.ceb.2016.08.002

Baldwin, A.T., J.H. Kim, H. Seo, and J.B. Wallingford. 2022a. Global analysis of cell behavior and protein dynamics reveals region-specific roles for Shroom3 and N-cadherin during neural tube closure. *Elife.* 11:e66704. https://doi.org/10.7554/eLife.66704

Baldwin, A.T., J.H. Kim, and J.B. Wallingford. 2022b. In vivo high-content imaging and regression analysis reveal non-cell autonomous functions of Shroom3 during neural tube closure. *Dev. Biol.* 491:105–112. https://doi.org/10.1016/j.ydbio.2022.08.011

Bellaïche, Y., A. Radovic, D.F. Woods, C.D. Hough, M.L. Parmentier, C.J. O'Kane, P.J. Bryant, and F. Schweisguth. 2001. The partner of inscuteable/Discs-large complex is required to establish planar polarity during asymmetric cell division in Drosophila. *Cell.* 106:355–366. https://doi.org/10.1016/S0092-8674(01)00444-5

Besson, C., F. Bernard, F. Corson, H. Rouault, E. Reynaud, A. Keder, K. Mazouni, and F. Schweisguth. 2015. Planar cell polarity breaks the symmetry of PAR protein distribution prior to mitosis in drosophila sensory organ precursor cells. *Curr. Biol.* 25:1104–1110. https://doi.org/10.1016/j.cub.2015.02.073

Bocanegra-Moreno, L., A. Singh, E. Hannezo, M. Zagorski, and A. Kicheva. 2023. Cell cycle dynamics control fluidity of the developing mouse neuroepithelium. *Nat. Phys.* 19:1050–1058. https://doi.org/10.1038/s41567-023-01977-w

Bosveld, F., and Y. Bellaïche. 2020. Tricellular junctions. *Curr. Biol.* 30: R249–R251. https://doi.org/10.1016/j.cub.2020.01.029

Bosveld, F., Z. Wang, and Y. Bellaïche. 2018. Tricellular junctions: A hot corner of epithelial biology. *Curr. Opin. Cell Biol.* 54:80–88. https://doi.org/10.1016/j.ceb.2018.05.002

Bouchet, J., I. Del Río-Iñiguez, R. Lasserre, S. Agüera-Gonzalez, C. Cuche, A. Danckaert, M.W. McCaffrey, V. Di Bartolo, and A. Alcover. 2016. Rac1-Rab11-FIP3 regulatory hub coordinates vesicle traffic with actin remodeling and T-cell activation. *EMBO J.* 35:1160–1174. https://doi.org/10.15252/embj.201593274

Burkel, B.M., G. von Dassow, and W.M. Bement. 2007. Versatile fluorescent probes for actin filaments based on the actin-binding domain of utrophin. *Cell Motil. Cytoskeleton.* 64:822–832. https://doi.org/10.1002/cm.20226

Burridge, K., and K. Wennerberg. 2004. Rho and Rac take center stage. *Cell.* 116:167–179. https://doi.org/10.1016/S0092-8674(04)00003-0

Butler, M.T., and J.B. Wallingford. 2015. Control of vertebrate core planar cell polarity protein localization and dynamics by Prickle 2. *Development.* 142:3429–3439.

Butler, M.T., and J.B. Wallingford. 2018. Spatial and temporal analysis of PCP protein dynamics during neural tube closure. *Elife.* 7:e36456. https://doi.org/10.7554/eLife.36456

Cardellini, P., A. Cirelli, and S. Citi. 2007. Tight junction formation in early Xenopus laevis embryos: Identification and ultrastructural characterization of junctional crests and junctional vesicles. *Cell Tissue Res.* 330: 247–256. https://doi.org/10.1007/s00441-007-0472-9

Carreira-Barbosa, F., M.L. Concha, M. Takeuchi, N. Ueno, S.W. Wilson, and M. Tada. 2003. Prickle 1 regulates cell movements during gastrulation and neuronal migration in zebrafish. *Development.* 130:4037–4046. https://doi.org/10.1242/dev.00567

Chauhan, B.K., M. Lou, Y. Zheng, and R.A. Lang. 2011. Balanced Rac1 and RhoA activities regulate cell shape and drive invagination morphogenesis in epithelia. *Proc. Natl. Acad. Sci. USA.* 108:18289–18294. https://doi.org/10.1073/pnas.1108993108

Chen, B., H.T. Chou, C.A. Brautigam, W. Xing, S. Yang, L. Henry, L.K. Doolittle, T. Walz, and M.K. Rosen. 2017. Rac1 GTPase activates the WAVE regulatory complex through two distinct binding sites. *Elife.* 6:e29795. https://doi.org/10.7554/eLife.29795

Chertkova, A.O., M. Mastop, M. Postma, N. van Bommel, S. van der Niet, K.L. Batenburg, L. Joosen, T.W.J. Gadella, Y. Okada, and J. Goedhart. 2020. Robust and bright genetically encoded fluorescent markers for highlighting structures and compartments in mammalian cells. *bioRxiv.* https://doi.org/10.1101/160374 (Preprint posted January 13, 2020).

Cho, B., G. Pierre-Louis, A. Sagner, S. Eaton, and J.D. Axelrod. 2015. Clustering and negative feedback by endocytosis in planar cell polarity signaling is modulated by ubiquitinylation of prickle. *PLoS Genet.* 11: e1005259. https://doi.org/10.1371/journal.pgen.1005259

Christodoulou, N., and P.A. Skourides. 2022. Distinct spatiotemporal contribution of morphogenetic events and mechanical tissue coupling during Xenopus neural tube closure. *Development.* 149:dev200358. https://doi.org/10.1242/dev.200358

Chuykin, I., O. Ossipova, and S.Y. Sokol. 2018. Par3 interacts with Prickle3 to generate apical PCP complexes in the vertebrate neural plate. *Elife.* 7: e37881. https://doi.org/10.7554/eLife.37881

Ciruna, B., A. Jenny, D. Lee, M. Mlodzik, and A.F. Schier. 2006. Planar cell polarity signalling couples cell division and morphogenesis during neurulation. *Nature*. 439:220–224. https://doi.org/10.1038/nature04375

Citi, S., D. Guerrera, D. Spadaro, and J. Shah. 2014. Epithelial junctions and Rho family GTPases: The zonular signalosome. *Small GTPases*. 5:1–15. https://doi.org/10.4161/21541248.2014.973760

Classen, A.K., K.I. Anderson, E. Marois, and S. Eaton. 2005. Hexagonal packing of Drosophila wing epithelial cells by the planar cell polarity pathway. *Dev. Cell*. 9:805–817. https://doi.org/10.1016/j.devcel.2005.10.016

Clausi, D.A., and G.W. Brodland. 1993. Mechanical evaluation of theories of neurulation using computer simulations. *Development*. 118:1013–1023. https://doi.org/10.1242/dev.118.3.1013

Colas, J.F., and G.C. Schoenwolf. 2001. Towards a cellular and molecular understanding of neurulation. *Dev. Dyn.* 221:117–145. https://doi.org/10.1002/dvdy.1144

Collinet, C., M. Rauzi, P.F. Lenne, and T. Lecuit. 2015. Local and tissue-scale forces drive oriented junction growth during tissue extension. *Nat. Cell Biol.* 17:1247–1258. https://doi.org/10.1038/ncb3226

Cox, E.P. 1927. A method of assigning numerical and percentage values to the degree of roundness of sand grains. *J. Paleontol.* 1:179–183.

Daneshjou, N., N. Sieracki, G.P. van Nieuw Amerongen, D.E. Conway, M.A. Schwartz, Y.A. Komarova, and A.B. Malik. 2015. Rac1 functions as a reversible tension modulator to stabilize VE-cadherin trans-interaction. *J. Cell Biol.* 208:23–32. https://doi.org/10.1083/jcb.201409108

Daulat, A.M., P. Finetti, D. Revinski, M. Silveira Wagner, L. Camoin, S. Audebert, D. Birnbaum, L. Kodjabachian, J.P. Borg, and F. Bertucci. 2019. ECT2 associated to PRICKLE1 are poor-prognosis markers in triple-negative breast cancer. *Br. J. Cancer*. 120:931–940. https://doi.org/10.1038/s41416-019-0448-z

Daulat, A.M., O. Luu, A. Sing, L. Zhang, J.L. Wrana, H. McNeill, R. Winklbauer, and S. Angers. 2012. Mink1 regulates β-catenin-independent Wnt signaling via prickle phosphorylation. *Mol. Cell. Biol.* 32:173–185. https://doi.org/10.1128/MCB.06320-11

Davey, C.F., and C.B. Moens. 2017. Planar cell polarity in moving cells: Think globally, act locally. *Development*. 144:187–200. https://doi.org/10.1242/dev.122804

David, D.J., Q. Wang, J.J. Feng, and T.J. Harris. 2013. Bazooka inhibits aPKC to limit antagonism of actomyosin networks during amnioserosa apical constriction. *Development*. 140:4719–4729. https://doi.org/10.1242/dev.098491

David, R., O. Luu, E.W. Damm, J.W. Wen, M. Nagel, and R. Winklbauer. 2014. Tissue cohesion and the mechanics of cell rearrangement. *Development*. 141:3672–3682. https://doi.org/10.1242/dev.104315

Davidson, L.A., and R.E. Keller. 1999. Neural tube closure in Xenopus laevis involves medial migration, directed protrusive activity, cell intercalation and convergent extension. *Development*. 126:4547–4556. https://doi.org/10.1242/dev.126.20.4547

Devany, J., D.M. Sussman, T. Yamamoto, M.L. Manning, and M.L. Gardel. 2021. Cell cycle-dependent active stress drives epithelia remodeling. *Proc. Natl. Acad. Sci. USA*. 118:e1917853118. https://doi.org/10.1073/pnas.1917853118

Devenport, D., and E. Fuchs. 2008. Planar polarization in embryonic epidermis orchestrates global asymmetric morphogenesis of hair follicles. *Nat. Cell Biol.* 10:1257–1268. https://doi.org/10.1038/ncb1784

Devitt, C.C., S. Weng, V.D. Bejar-Padilla, J. Alvarado, and J.B. Wallingford. 2024. PCP and Septins govern the polarized organization of the actin cytoskeleton during convergent extension. *Curr. Biol.* 34:615–622.e4. https://doi.org/10.1016/j.cub.2023.12.025

Diez Del Corral, R., and A.V. Morales. 2017. The multiple roles of FGF signaling in the developing spinal cord. *Front. Cell Dev. Biol.* 5:58. https://doi.org/10.3389/fcell.2017.00058

Edri, T., D. Cohen, Y. Shabtai, and A. Fainsod. 2023. Alcohol induces neural tube defects by reducing retinoic acid signaling and promoting neural plate expansion. *Front. Cell Dev. Biol.* 11:1282273. https://doi.org/10.3389/fcell.2023.1282273

Erasmus, J.C., K. Smolarczyk, H. Brezovjakova, N.F. Mohd-Naim, E. Lozano, K. Matter, and V.M.M. Braga. 2021. Rac1-PAK1 regulation of Rab11 cycling promotes junction destabilization. *J. Cell Biol.* 220:e202002114. https://doi.org/10.1083/jcb.202002114

Erasmus, J.C., N.J. Welsh, and V.M. Braga. 2015. Cooperation of distinct Rac-dependent pathways to stabilise E-cadherin adhesion. *Cell. Signal.* 27:1905–1913. https://doi.org/10.1016/j.cellsig.2015.04.014

Farhadifar, R., J.C. Röper, B. Aigouy, S. Eaton, and F. Jülicher. 2007. The influence of cell mechanics, cell-cell interactions, and proliferation on epithelial packing. *Curr. Biol.* 17:2095–2104. https://doi.org/10.1016/j.cub.2007.11.049

Fesenko, I., T. Kurth, B. Sheth, T.P. Fleming, S. Citi, and P. Hausen. 2000. Tight junction biogenesis in the early Xenopus embryo. *Mech. Dev.* 96:51–65. https://doi.org/10.1016/S0925-4773(00)00368-3

Finegan, T.M., N. Hervieux, A. Nestor-Bergmann, A.G. Fletcher, G.B. Blanchard, and B. Sanson. 2019. The tricellular vertex-specific adhesion molecule Sidekick facilitates polarised cell intercalation during Drosophila axis extension. *PLoS Biol.* 17:e3000522. https://doi.org/10.1371/journal.pbio.3000522

Firmino, J., D. Rocancourt, M. Saadaoui, C. Moreau, and J. Gros. 2016. Cell division drives epithelial cell rearrangements during gastrulation in chick. *Dev. Cell*. 36:249–261. https://doi.org/10.1016/j.devcel.2016.01.007

Founounou, N., R. Farhadifar, G.M. Collu, U. Weber, M.J. Shelley, and M. Mlodzik. 2021. Tissue fluidity mediated by adherens junction dynamics promotes planar cell polarity-driven ommatidial rotation. *Nat. Commun.* 12:6974. https://doi.org/10.1038/s41467-021-27253-0

Frasa, M.A., F.C. Maximiano, K. Smolarczyk, R.E. Francis, M.E. Betson, E. Lozano, J. Goldenring, M.C. Seabra, A. Rak, M.R. Ahmadian, and V.M. Braga. 2010. Armus is a Rac1 effector that inactivates Rab7 and regulates E-cadherin degradation. *Curr. Biol.* 20:198–208. https://doi.org/10.1016/j.cub.2009.12.053

Galea, G.L., E. Maniou, T.J. Edwards, A.R. Marshall, I. Ampartzidis, N.D.E. Greene, and A.J. Copp. 2021. Cell non-autonomy amplifies disruption of neurulation by mosaic Vangl2 deletion in mice. *Nat. Commun.* 12:1159. https://doi.org/10.1038/s41467-021-21372-4

Goodrich, L.V.L., and D. Strutt. 2011. Principles of planar polarity in animal development. *Development*. 138:1877–1892. https://doi.org/10.1242/dev.054080

Gray, R.S., I. Roszko, and L. Solnica-Krezel. 2011. Planar cell polarity: Coordinating morphogenetic cell behaviors with embryonic polarity. *Dev. Cell*. 21:120–133. https://doi.org/10.1016/j.devcel.2011.06.011

Grikscheit, K., T. Frank, Y. Wang, and R. Grosse. 2015. Junctional actin assembly is mediated by Formin-like 2 downstream of Rac1. *J. Cell Biol.* 209:367–376. https://doi.org/10.1083/jcb.201412015

Guillot, C., and T. Lecuit. 2013. Mechanics of epithelial tissue homeostasis and morphogenesis. *Science*. 340:1185–1189. https://doi.org/10.1126/science.1235249

Habas, R., Y. Kato, and X. He. 2001. Wnt/Frizzled activation of Rho regulates vertebrate gastrulation and requires a novel Formin homology protein Daam1. *Cell*. 107:843–854. https://doi.org/10.1016/S0092-8674(01)00614-6

Hall, A. 1998. Rho GTPases and the actin cytoskeleton. *Science*. 279:509–514. https://doi.org/10.1126/science.279.5350.509

Handler, C., G. Scarcelli, and J. Zhang. 2023. Time-lapse mechanical imaging of neural tube closure in live embryo using Brillouin microscopy. *Sci. Rep.* 13:263. https://doi.org/10.1038/s41598-023-27456-z

Harland, R.M. 1991. In situ hybridization: An improved whole-mount method for Xenopus embryos. *Methods Cell Biol.* 36:685–695. https://doi.org/10.1016/S0091-679X(08)60307-6

Hashimoto, H., F.B. Robin, K.M. Sherrard, and E.M. Munro. 2015. Sequential contraction and exchange of apical junctions drives zippering and neural tube closure in a simple chordate. *Dev. Cell*. 32:241–255. https://doi.org/10.1016/j.devcel.2014.12.017

Heasman, S.J., and A.J. Ridley. 2008. Mammalian Rho GTPases: New insights into their functions from in vivo studies. *Nat. Rev. Mol. Cell Biol.* 9:690–701. https://doi.org/10.1038/nrm2476

Henderson, D.J., D.A. Long, and C.H. Dean. 2018. Planar cell polarity in organ formation. *Curr. Opin. Cell Biol.* 55:96–103. https://doi.org/10.1016/j.ceb.2018.06.011

Herbomel, G., G. Hatte, J. Roul, S. Padilla-Parra, J.P. Tassan, and M. Tramier. 2017. Actomyosin-generated tension on cadherin is similar between dividing and non-dividing epithelial cells in early Xenopus laevis embryos. *Sci. Rep.* 7:45058. https://doi.org/10.1038/srep45058

Higashi, T., T.R. Arnold, R.E. Stephenson, K.M. Dinshaw, and A.L. Miller. 2016. Maintenance of the epithelial barrier and remodeling of cell-cell junctions during cytokinesis. *Curr. Biol.* 26:1829–1842. https://doi.org/10.1016/j.cub.2016.05.036

Hirano, S., Y. Mii, G. Charras, and T. Michiue. 2022. Alignment of the cell long axis by unidirectional tension acts cooperatively with Wnt signalling to establish planar cell polarity. *Development*. 149:dev200515. https://doi.org/10.1242/dev.200515

Huang, Y., and R. Winklbauer. 2022. Cell cortex regulation by the planar cell polarity protein Prickle1. *J. Cell Biol.* 221:e202008116. https://doi.org/10.1083/jcb.202008116

Huebner, R.J., A.N. Malmi-Kakkada, S. Sarıkaya, S. Weng, D. Thirumalai, and J.B. Wallingford. 2021. Mechanical heterogeneity along single cell-cell

junctions is driven by lateral clustering of cadherins during vertebrate axis elongation. *Elife*. 10:e65390. https://doi.org/10.7554/eLife.65390
Humphries, A.C., and M. Mlodzik. 2018. From instruction to output: Wnt/PCP signaling in development and cancer. *Curr. Opin. Cell Biol.* 51:110–116. https://doi.org/10.1016/j.ceb.2017.12.005
Ikenouchi, J., M. Furuse, K. Furuse, H. Sasaki, S. Tsukita, and S. Tsukita. 2005. Tricellulin constitutes a novel barrier at tricellular contacts of epithelial cells. *J. Cell Biol.* 171:939–945. https://doi.org/10.1083/jcb.200510043
Ishiuchi, T., and M. Takeichi. 2011. Willin and Par3 cooperatively regulate epithelial apical constriction through aPKC-mediated ROCK phosphorylation. *Nat. Cell Biol.* 13:860–866. https://doi.org/10.1038/ncb2274
Izumi, G., T. Sakisaka, T. Baba, S. Tanaka, K. Morimoto, and Y. Takai. 2004. Endocytosis of E-cadherin regulated by Rac and Cdc42 small G proteins through IQGAP1 and actin filaments. *J. Cell Biol.* 166:237–248. https://doi.org/10.1083/jcb.200401078
Jenny, A., R.S. Darken, P.A. Wilson, and M. Mlodzik. 2003. Prickle and Strabismus form a functional complex to generate a correct axis during planar cell polarity signaling. *EMBO J.* 22:4409–4420. https://doi.org/10.1093/emboj/cdg424
Keller, R. 2002. Shaping the vertebrate body plan by polarized embryonic cell movements. *Science*. 298:1950–1954. https://doi.org/10.1126/science.1079478
Keller, R. 2012. Developmental biology. Physical biology returns to morphogenesis. *Science*. 338:201–203. https://doi.org/10.1126/science.1230718
Kim, S., M. Pochitaloff, G.A. Stooke-Vaughan, and O. Campàs. 2021. Embryonic tissues as active foams. *Nat. Phys.* 17:859–866. https://doi.org/10.1038/s41567-021-01215-1
Kowalczyk, A.P., and B.A. Nanes. 2012. Adherens junction turnover: Regulating adhesion through cadherin endocytosis, degradation, and recycling. *Subcell. Biochem.* 60:197–222. https://doi.org/10.1007/978-94-007-4186-7_9
Kuriyama, S., E. Theveneau, A. Benedetto, M. Parsons, M. Tanaka, G. Charras, A. Kabla, and R. Mayor. 2014. In vivo collective cell migration requires an LPAR2-dependent increase in tissue fluidity. *J. Cell Biol.* 206:113–127. https://doi.org/10.1083/jcb.201402093
Lawton, A.K., A. Nandi, M.J. Stulberg, N. Dray, M.W. Sneddon, W. Pontius, T. Emonet, and S.A. Holley. 2013. Regulated tissue fluidity steers zebrafish body elongation. *Development*. 140:573–582. https://doi.org/10.1242/dev.090381
Letizia, A., D. He, S. Astigarraga, J. Colombelli, V. Hatini, M. Llimargas, and J.E. Treisman. 2019. Sidekick is a key component of tricellular adherens junctions that acts to resolve cell rearrangements. *Dev. Cell*. 50:313–326.e5. https://doi.org/10.1016/j.devcel.2019.07.007
Mancini, P., O. Ossipova, and S.Y. Sokol. 2021. The dorsal blastopore lip is a source of signals inducing planar cell polarity in the Xenopus neural plate. *Biol. Open*. 10:bio058761. https://doi.org/10.1242/bio.058761
Mao, Y., and S.A. Wickström. 2024. Mechanical state transitions in the regulation of tissue form and function. *Nat. Rev. Mol. Cell Biol.* 25:654–670. https://doi.org/10.1038/s41580-024-00719-x
Martin, A.C., M. Gelbart, R. Fernandez-Gonzalez, M. Kaschube, and E.F. Wieschaus. 2010. Integration of contractile forces during tissue invagination. *J. Cell Biol.* 188:735–749. https://doi.org/10.1083/jcb.200910099
Matoz-Fernandez, D.A., K. Martens, R. Sknepnek, J.L. Barrat, and S. Henkes. 2017. Cell division and death inhibit glassy behaviour of confluent tissues. *Soft Matter*. 13:3205–3212. https://doi.org/10.1039/C6SM02580C
Matsuda, M., A. Kubo, M. Furuse, and S. Tsukita. 2004. A peculiar internalization of claudins, tight junction-specific adhesion molecules, during the intercellular movement of epithelial cells. *J. Cell Sci.* 117:1247–1257. https://doi.org/10.1242/jcs.00972
Matsuda, M., J. Rozman, S. Ostvar, K.E. Kasza, and S.Y. Sokol. 2023. Mechanical control of neural plate folding by apical domain alteration. *Nat. Commun.* 14:8475. https://doi.org/10.1038/s41467-023-43973-x
McCormack, J., N.J. Welsh, and V.M. Braga. 2013. Cycling around cell-cell adhesion with Rho GTPase regulators. *J. Cell Sci.* 126:379–391. https://doi.org/10.1242/jcs.097923
McGreevy, E.M., D. Vijayraghavan, L.A. Davidson, and J.D. Hildebrand. 2015. Shroom3 functions downstream of planar cell polarity to regulate myosin II distribution and cellular organization during neural tube closure. *Biol. Open*. 4:186–196. https://doi.org/10.1242/bio.20149589
Mitchel, J.A., A. Das, M.J. O'Sullivan, I.T. Stancil, S.J. DeCamp, S. Koehler, O.H. Ocaña, J.P. Butler, J.J. Fredberg, M.A. Nieto, et al. 2020. In primary airway epithelial cells, the unjamming transition is distinct from the epithelial-to-mesenchymal transition. *Nat. Commun.* 11:5053. https://doi.org/10.1038/s41467-020-18841-7
Mongera, A., P. Rowghanian, H.J. Gustafson, E. Shelton, D.A. Kealhofer, E.K. Carn, F. Serwane, A.A. Lucio, J. Giammona, and O. Campàs. 2018. A fluid-to-solid jamming transition underlies vertebrate body axis elongation. *Nature*. 561:401–405. https://doi.org/10.1038/s41586-018-0479-2
Montcouquiol, M., R.A. Rachel, P.J. Lanford, N.G. Copeland, N.A. Jenkins, and M.W. Kelley. 2003. Identification of Vangl2 and Scrb1 as planar polarity genes in mammals. *Nature*. 423:173–177. https://doi.org/10.1038/nature01618
Moon, L.D., and F. Xiong. 2022. Mechanics of neural tube morphogenesis. *Semin. Cell Dev. Biol.* 130:56–69. https://doi.org/10.1016/j.semcdb.2021.09.009
Msibi, Z.N.P., and M.V. Mabandla. 2019. Oleanolic acid mitigates 6-hydroxydopamine neurotoxicity by attenuating intracellular ROS in PC12 cells and striatal microglial activation in rat brains. *Front. Physiol.* 10:1059. https://doi.org/10.3389/fphys.2019.01059
Nagaoka, T., R. Ohashi, A. Inutsuka, S. Sakai, N. Fujisawa, M. Yokoyama, Y.H. Huang, M. Igarashi, and M. Kishi. 2014. The Wnt/planar cell polarity pathway component Vangl2 induces synapse formation through direct control of N-cadherin. *Cell Rep.* 6:916–927. https://doi.org/10.1016/j.celrep.2014.01.044
Nelson, W.J. 2009. Remodeling epithelial cell organization: Transitions between front-rear and apical-basal polarity. *Cold Spring Harb. Perspect. Biol.* 1:a000513. https://doi.org/10.1101/cshperspect.a000513
Niederreither, K., V. Subbarayan, P. Dollé, and P. Chambon. 1999. Embryonic retinoic acid synthesis is essential for early mouse post-implantation development. *Nat. Genet.* 21:444–448. https://doi.org/10.1038/7788
Nieuwkoop, P.D., and J. Faber. 1994. Normal Table of Xenopus laevis (Daudin): A Systematical and Chronological Survey of the Development from the Fertilized Egg Till the End of Metamorphosis. Garland Publishing, New York, NY, USA. 252.
Nishimura, T., H. Honda, and M. Takeichi. 2012. Planar cell polarity links axes of spatial dynamics in neural-tube closure. *Cell*. 149:1084–1097. https://doi.org/10.1016/j.cell.2012.04.021
Nordström, U., T.M. Jessell, and T. Edlund. 2002. Progressive induction of caudal neural character by graded Wnt signaling. *Nat. Neurosci.* 5:525–532. https://doi.org/10.1038/nn0602-854
Ossipova, O., C.W. Chu, J. Fillatre, B.K. Brott, K. Itoh, and S.Y. Sokol. 2015a. The involvement of PCP proteins in radial cell intercalations during Xenopus embryonic development. *Dev. Biol.* 408:316–327. https://doi.org/10.1016/j.ydbio.2015.06.013
Ossipova, O., I. Chuykin, C.W. Chu, and S.Y. Sokol. 2015b. Vangl2 cooperates with Rab11 and Myosin V to regulate apical constriction during vertebrate gastrulation. *Development*. 142:99–107. https://doi.org/10.1242/dev.111161
Ossipova, O., K. Kim, B.B. Lake, K. Itoh, A. Ioannou, and S.Y. Sokol. 2014. Role of Rab11 in planar cell polarity and apical constriction during vertebrate neural tube closure. *Nat. Commun.* 5:3734. https://doi.org/10.1038/ncomms4734
Ossipova, O., K. Kim, and S.Y. Sokol. 2015c. Planar polarization of Vangl2 in the vertebrate neural plate is controlled by Wnt and Myosin II signaling. *Biol. Open*. 4:722–730. https://doi.org/10.1242/bio.201511676
Pachitariu, M., and C. Stringer. 2022. Cellpose 2.0: How to train your own model. *Nat. Methods*. 19:1634–1641. https://doi.org/10.1038/s41592-022-01663-4
Park, J.A., and J.J. Fredberg. 2016. Cell jamming in the airway epithelium. *Ann. Am. Thorac. Soc.* 13:S64–S67. https://doi.org/10.1513/AnnalsATS.201507-476MG
Peng, H.B. 1991. Xenopus laevis: Practical uses in cell and molecular biology. Solutions and protocols. *Methods Cell Biol.* 36:657–662.
Peng, Y., and J.D. Axelrod. 2012. Asymmetric protein localization in planar cell polarity: Mechanisms, puzzles, and challenges. *Curr. Top. Dev. Biol.* 101:33–53. https://doi.org/10.1016/B978-0-12-394592-1.00002-8
Pinheiro, D., and Y. Bellaïche. 2018. Mechanical force-driven adherens junction remodeling and epithelial dynamics. *Dev. Cell*. 47:3–19. https://doi.org/10.1016/j.devcel.2018.09.014
Ranft, J., M. Basan, J. Elgeti, J.F. Joanny, J. Prost, and F. Jülicher. 2010. Fluidization of tissues by cell division and apoptosis. *Proc. Natl. Acad. Sci. USA*. 107:20863–20868. https://doi.org/10.1073/pnas.1011086107
Rauzi, M., P.F. Lenne, and T. Lecuit. 2010. Planar polarized actomyosin contractile flows control epithelial junction remodelling. *Nature*. 468:1110–1114. https://doi.org/10.1038/nature09566
Rauzi, M., P. Verant, T. Lecuit, and P.F. Lenne. 2008. Nature and anisotropy of cortical forces orienting Drosophila tissue morphogenesis. *Nat. Cell Biol.* 10:1401–1410. https://doi.org/10.1038/ncb1798
Röper, K. 2013. Supracellular actomyosin assemblies during development. *Bioarchitecture*. 3:45–49. https://doi.org/10.4161/bioa.25339
Sawyer, J.K., W. Choi, K.C. Jung, L. He, N.J. Harris, and M. Peifer. 2011. A contractile actomyosin network linked to adherens junctions by

Canoe/afadin helps drive convergent extension. *Mol. Biol. Cell*. 22: 2491–2508. https://doi.org/10.1091/mbc.e11-05-0411

Shindo, A., Y. Inoue, M. Kinoshita, and J.B. Wallingford. 2019. PCP-dependent transcellular regulation of actomyosin oscillation facilitates convergent extension of vertebrate tissue. *Dev. Biol.* 446:159–167. https://doi.org/10.1016/j.ydbio.2018.12.017

Simões, S.M., J.T. Blankenship, O. Weitz, D.L. Farrell, M. Tamada, R. Fernandez-Gonzalez, and J.A. Zallen. 2010. Rho-kinase directs Bazooka/Par-3 planar polarity during Drosophila axis elongation. *Dev. Cell*. 19: 377–388. https://doi.org/10.1016/j.devcel.2010.08.011

Smith, J.L., and G.C. Schoenwolf. 1997. Neurulation: Coming to closure. *Trends Neurosci.* 20:510–517. https://doi.org/10.1016/S0166-2236(97)01121-1

Sokol, S.Y. 1996. Analysis of dishevelled signalling pathways during Xenopus development. *Curr. Biol.* 6:1456–1467. https://doi.org/10.1016/S0960-9822(96)00750-6

Sokol, S.Y. 2016. Mechanotransduction during vertebrate neurulation. *Curr. Top. Dev. Biol.* 117:359–376. https://doi.org/10.1016/bs.ctdb.2015.11.036

Storey, K.G., A. Goriely, C.M. Sargent, J.M. Brown, H.D. Burns, H.M. Abud, and J.K. Heath. 1998. Early posterior neural tissue is induced by FGF in the chick embryo. *Development*. 125:473–484. https://doi.org/10.1242/dev.125.3.473

Takeuchi, M., J. Nakabayashi, T. Sakaguchi, T.S. Yamamoto, H. Takahashi, H. Takeda, and N. Ueno. 2003. The prickle-related gene in vertebrates is essential for gastrulation cell movements. *Curr. Biol.* 13:674–679. https://doi.org/10.1016/S0960-9822(03)00245-8

Tao, H., M. Suzuki, H. Kiyonari, T. Abe, T. Sasaoka, and N. Ueno. 2009. Mouse prickle1, the homolog of a PCP gene, is essential for epiblast apical-basal polarity. *Proc. Natl. Acad. Sci. USA*. 106:14426–14431. https://doi.org/10.1073/pnas.0901332106

Tetley, R.J., and Y. Mao. 2018. The same but different: Cell intercalation as a driver of tissue deformation and fluidity. *Philos. Trans. R. Soc. Lond. B Biol. Sci.* 373:20170328. https://doi.org/10.1098/rstb.2017.0328

Timmerman, I., N. Heemskerk, J. Kroon, A. Schaefer, J. van Rijssel, M. Hoogenboezem, J. van Unen, J. Goedhart, T.W. Gadella Jr., T. Yin, et al. 2015. A local VE-cadherin and Trio-based signaling complex stabilizes endothelial junctions through Rac1. *J. Cell Sci.* 128:3041–3054. https://doi.org/10.1242/jcs.179424

Uechi, H., and E. Kuranaga. 2019. The Tricellular junction protein sidekick regulates vertex dynamics to promote bicellular junction extension. *Dev. Cell*. 50:327–338.e5. https://doi.org/10.1016/j.devcel.2019.06.017

Ulicna, K., G. Vallardi, G. Charras, and A.R. Lowe. 2021. Automated deep lineage tree analysis using a bayesian single cell tracking approach. *Front. Comput. Sci.* 3:734559. https://doi.org/10.3389/fcomp.2021.734559

Vanderleest, T.E., C.M. Smits, Y. Xie, C.E. Jewett, J.T. Blankenship, and D. Loerke. 2018. Vertex sliding drives intercalation by radial coupling of adhesion and actomyosin networks during Drosophila germband extension. *Elife*. 7:e34586. https://doi.org/10.7554/eLife.34586

Veeman, M.T., D.C. Slusarski, A. Kaykas, S.H. Louie, and R.T. Moon. 2003. Zebrafish prickle, a modulator of noncanonical Wnt/Fz signaling, regulates gastrulation movements. *Curr. Biol.* 13:680–685. https://doi.org/10.1016/S0960-9822(03)00240-9

Vielemeyer, O., C. Nizak, A.J. Jimenez, A. Echard, B. Goud, J. Camonis, J.C. Rain, and F. Perez. 2010. Characterization of single chain antibody targets through yeast two hybrid. *BMC Biotechnol.* 10:59. https://doi.org/10.1186/1472-6750-10-59

Wallingford, J.B., S.E. Fraser, and R.M. Harland. 2002. Convergent extension: The molecular control of polarized cell movement during embryonic development. *Dev. Cell*. 2:695–706. https://doi.org/10.1016/S1534-5807(02)00197-1

Wang, X., M. Merkel, L.B. Sutter, G. Erdemci-Tandogan, M.L. Manning, and K.E. Kasza. 2020. Anisotropy links cell shapes to tissue flow during convergent extension. *Proc. Natl. Acad. Sci. USA*. 117:13541–13551. https://doi.org/10.1073/pnas.1916418117

Wang, Y.C., Z. Khan, M. Kaschube, and E.F. Wieschaus. 2012. Differential positioning of adherens junctions is associated with initiation of epithelial folding. *Nature*. 484:390–393. https://doi.org/10.1038/nature10938

Watanabe, T., K. Sato, and K. Kaibuchi. 2009. Cadherin-mediated intercellular adhesion and signaling cascades involving small GTPases. *Cold Spring Harb. Perspect. Biol.* 1:a003020. https://doi.org/10.1101/cshperspect.a003020

Wayt, J., A. Cartagena-Rivera, D. Dutta, J.G. Donaldson, and C.M. Waterman. 2021. Myosin II isoforms promote internalization of spatially distinct clathrin-independent endocytosis cargoes through modulation of cortical tension downstream of ROCK2. *Mol. Biol. Cell*. 32:226–236. https://doi.org/10.1091/mbc.E20-07-0480

Williams, M., W. Yen, X. Lu, and A. Sutherland. 2014. Distinct apical and basolateral mechanisms drive planar cell polarity-dependent convergent extension of the mouse neural plate. *Dev. Cell*. 29:34–46. https://doi.org/10.1016/j.devcel.2014.02.007

Woichansky, I., C.A. Beretta, N. Berns, and V. Riechmann. 2016. Three mechanisms control E-cadherin localization to the zonula adherens. *Nat. Commun.* 7:10834. https://doi.org/10.1038/ncomms10834

Xiong, F., W. Ma, B. Bénazéraf, L. Mahadevan, and O. Pourquié. 2020. Mechanical coupling coordinates the co-elongation of axial and paraxial tissues in avian embryos. *Dev. Cell*. 55:354–366.e5. https://doi.org/10.1016/j.devcel.2020.08.007

Yamaguchi, T.P. 2001. Heads or tails: Wnts and anterior-posterior patterning. *Curr. Biol.* 11:R713–R724. https://doi.org/10.1016/S0960-9822(01)00417-1

Ybot-Gonzalez, P., D. Savery, D. Gerrelli, M. Signore, C.E. Mitchell, C.H. Faux, N.D. Greene, and A.J. Copp. 2007. Convergent extension, planar-cell-polarity signalling and initiation of mouse neural tube closure. *Development*. 134:789–799. https://doi.org/10.1242/dev.000380

Yin, C., M. Kiskowski, P.A. Pouille, E. Farge, and L. Solnica-Krezel. 2008. Cooperation of polarized cell intercalations drives convergence and extension of presomitic mesoderm during zebrafish gastrulation. *J. Cell Biol.* 180:221–232. https://doi.org/10.1083/jcb.200704150

Yoon, J., J. Sun, M. Lee, Y.S. Hwang, and I.O. Daar. 2023. Wnt4 and ephrinB2 instruct apical constriction via Dishevelled and non-canonical signaling. *Nat. Commun.* 14:337. https://doi.org/10.1038/s41467-023-35991-6

Yu, J.C., and R. Fernandez-Gonzalez. 2016. Local mechanical forces promote polarized junctional assembly and axis elongation in Drosophila. *Elife*. 5: e10757. https://doi.org/10.7554/eLife.10757

Zanier, E.R., S. Fumagalli, C. Perego, F. Pischiutta, and M.G. De Simoni. 2015. Shape descriptors of the "never resting" microglia in three different acute brain injury models in mice. *Intensive Care Med. Exp.* 3:39. https://doi.org/10.1186/s40635-015-0039-0

Zhang, L., V. Luga, S.K. Armitage, M. Musiol, A. Won, C.M. Yip, S.V. Plotnikov, and J.L. Wrana. 2016. A lateral signalling pathway coordinates shape volatility during cell migration. *Nat. Commun.* 7:11714. https://doi.org/10.1038/ncomms11714

Zhang, L., and J.L. Wrana. 2018. Regulation of Rho GTPases from the lateral sides of migrating cells. *Small GTPases*. 9:345–348. https://doi.org/10.1080/21541248.2016.1234430

Zhou, J., S. Pal, S. Maiti, and L.A. Davidson. 2015. Force production and mechanical accommodation during convergent extension. *Development*. 142:692–701. https://doi.org/10.1242/dev.116533

JCB

# Supplemental material

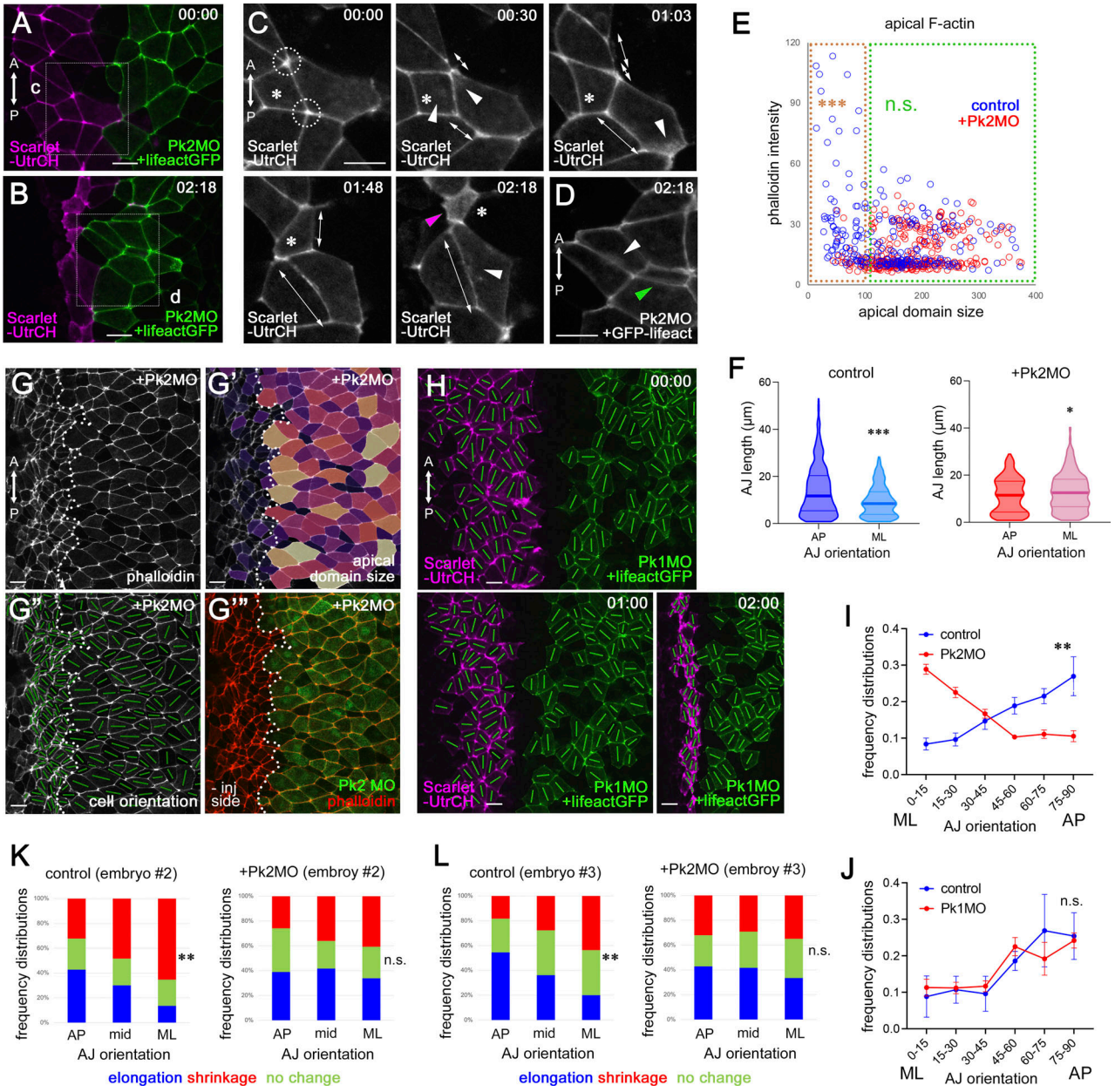


Figure S1. **Pk2 KD inhibits AP cell orientation in the NE. (A–D)** Snapshot images of F-actin distribution during cell intercalation and apical constriction in control NEs expressing Scarlet-UtrCH (purple) and Pk2-KD NEs expressing Lifeact-GFP (green). The white rectangular areas in A and B are enlarged in C and D. White circles indicate T1 junctions. The double arrows show AP elongation of newly formed AJs in the control NE. The white arrowheads indicate short-lived F-actin meshwork at the apical cortex. The purple arrowhead indicates stable F-actin enrichment at the apical cortex in apically constricted cells. Note the presence of short-lived apical F-actin but the absence of cells with stable apical F-actin in the Pk2 KD NE (D). **(E)** 2D plots representing F-actin abundance at the apical cortex in the control (blue) and Pk2-KD (red) NEs. The x axis represents the apical domain size of individual cells. The y axis represents the integrated fluorescence intensity of phalloidin staining. Dots represent individual cells. 234 cells (control) and 331 cells (Pk2 MO) from three embryos per group were used. Statistical analysis was conducted on two categorized cell populations: cells with small apical domains (<100 $\mu m^2$) and cells with large apical domains (>100 $\mu m^2$). The Mann–Whitney test was used to compare ranks between two groups. **(F)** Lengths of anteroposteriorly or mediolaterally oriented AJs in the control (left) and Pk2 KD (right) NEs. AJs were categorized into AP (≤30° from the AP axis) and ML (≤30° from the ML axis). The bold and thin lines indicate medians and quartiles, respectively. The Mann–Whitney test was used to compare mean ranks. $n$ = 339 (control, AP); $n$ = 209 (control, ML); $n$ = 233 (Pk2 KD, AP); $n$ = 402 (Pk2 KD, ML). Three embryos per group were used. **(G–G‴)** Representative images of phalloidin-stained NE. The control is on the left. Pk2 KD is on the right. Phalloidin staining only (G), overlaid with color coding on the basis of the apical domain size (G′), with the green bars indicating cell orientation (G″), and with GFP indicating Pk2 MO cells (G‴). **(H)** Snapshot images of the NE expressing Scarlet-UtrCH only (left) and Lifeact-GFP coinjected with Pk1 MO (right) from time-lapse imaging. The green lines represent the orientation of individual cells. **(I and J)** Frequency distribution histogram of cell orientation in the control (blue), Pk2 KD (red in J), and Pk1 KD (red in K) NEs. Averages and ±S.Ds. are shown. The Kolmogorov–Smirnov test was used to compare distributions. Three embryos per group were used. The total number of cells was as follows: $n$ = 920 (control in I), $n$ = 1,093 (Pk2 KD in I), $n$ = 120 (control in J), and $n$ = 130 (Pk1 KD in J). **(K and L)** Quantification of AJ length change and orientation in the control NEs (left) and Pk2 MO NEs (right). The statistical analyses were conducted as described in Fig. 2 H. 15 AJs per embryo were used. The total number of AJ length changes was as follows: $n$ = 353 (control in K), $n$ = 595 (Pk2 KD in K), $n$ = 171 (control in L), and $n$ = 195 (Pk2 KD in L). *P < 0.05, **P < 0.01, ***P < 0.001, n.s., not significant. Scale bars: 20 μm.

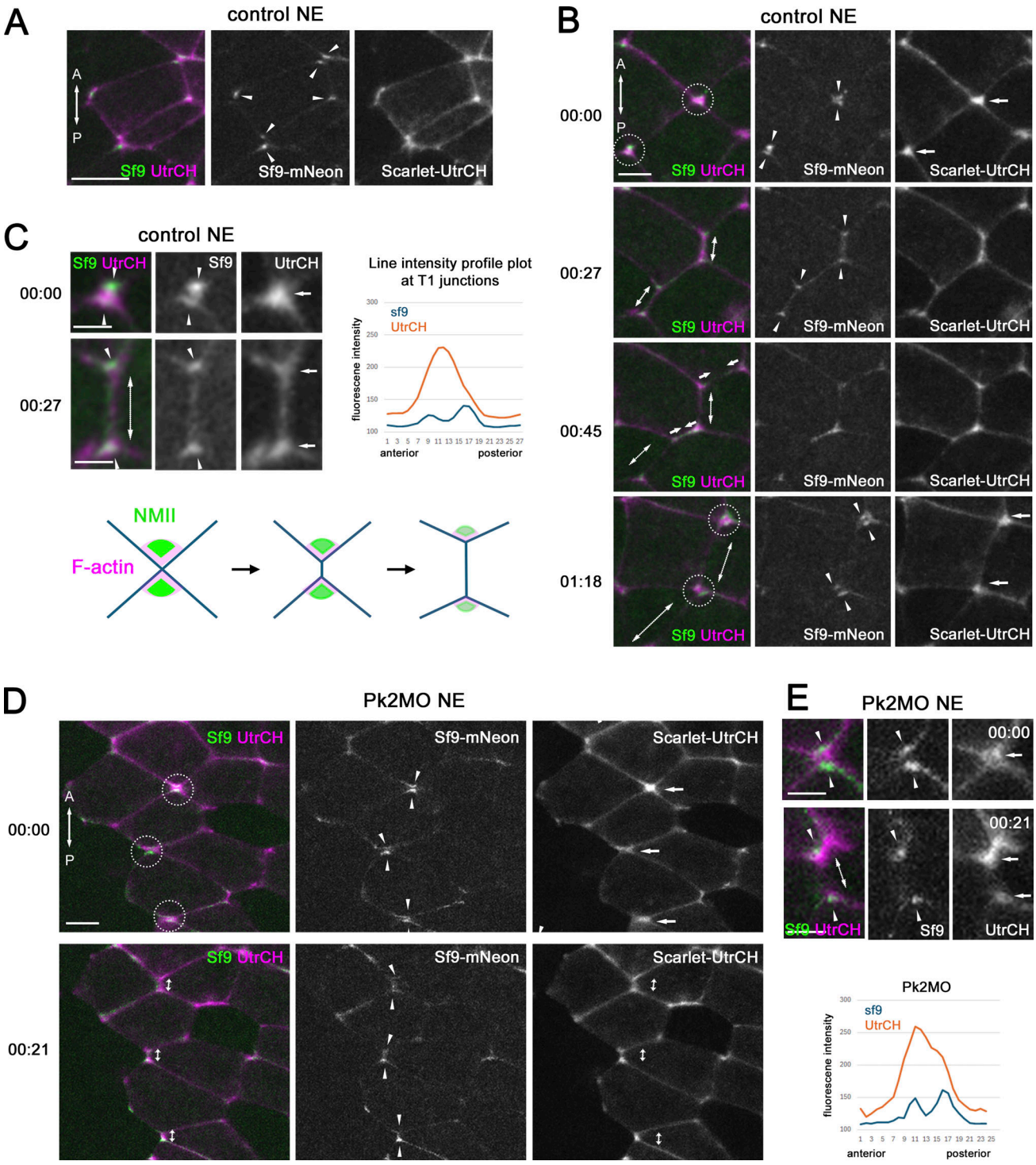


Figure S2. **Asymmetrical actomyosin network formation during T1 transition and AJ elongation. (A–C)** Representative images of wild-type NE cells expressing sf9-mNeonGreen and Scarlet-UtrCH. The white arrowheads indicate the accumulation of sf9-mNeon at tricellular vertices. **(B)** Representative snapshot images of NMII and F-actin during T1 transition and AP elongation of newly formed AJs from Video 5. The white circles represent T1 junctions. The arrowheads indicate crescent-shaped sf9 accumulation at the anterior and posterior sides of T1 junctions and retaining accumulation at the same vertices. The double arrows represent elongating AP junctions. The paired arrows represent shrinking ML junctions prior to the formation of T1 junctions. **(C)** Enlarged images of sf9-mNeonGreen and Scarlet-UtrCH at T1 junctions (left, top panel) or vertices on both ends of elongating AP junctions (left, middle panels). A line intensity profile plot shows two sf9 peaks and a single UtrCH peak at T1 junction (right panel). Schematic of NMII and actomyosin distribution during the T1 transition (bottom panel). **(D)** Representative snapshot images of sf9-mNeonGreen and Scarlet-UtrCH during T1 transition in Pk2-KD NEs from Video 5. The white circles represent T1 junctions. The arrowheads represent the accumulation of crescent-shaped sf9 at the anterior and posterior sides of T1 junction and the remaining accumulation at both ends of elongating AP junctions. The double arrows represent elongating AP junctions. **(E)** Enlarged images of representative T1 junctions (top panels) and newly formed AP junctions (middle panels). Line intensity profile plot of T1 junctions in the Pk2 KD NE (bottom panel). Scale bars: 10 µm in A, 5 µm in B and D, and 2 µm in C and E.

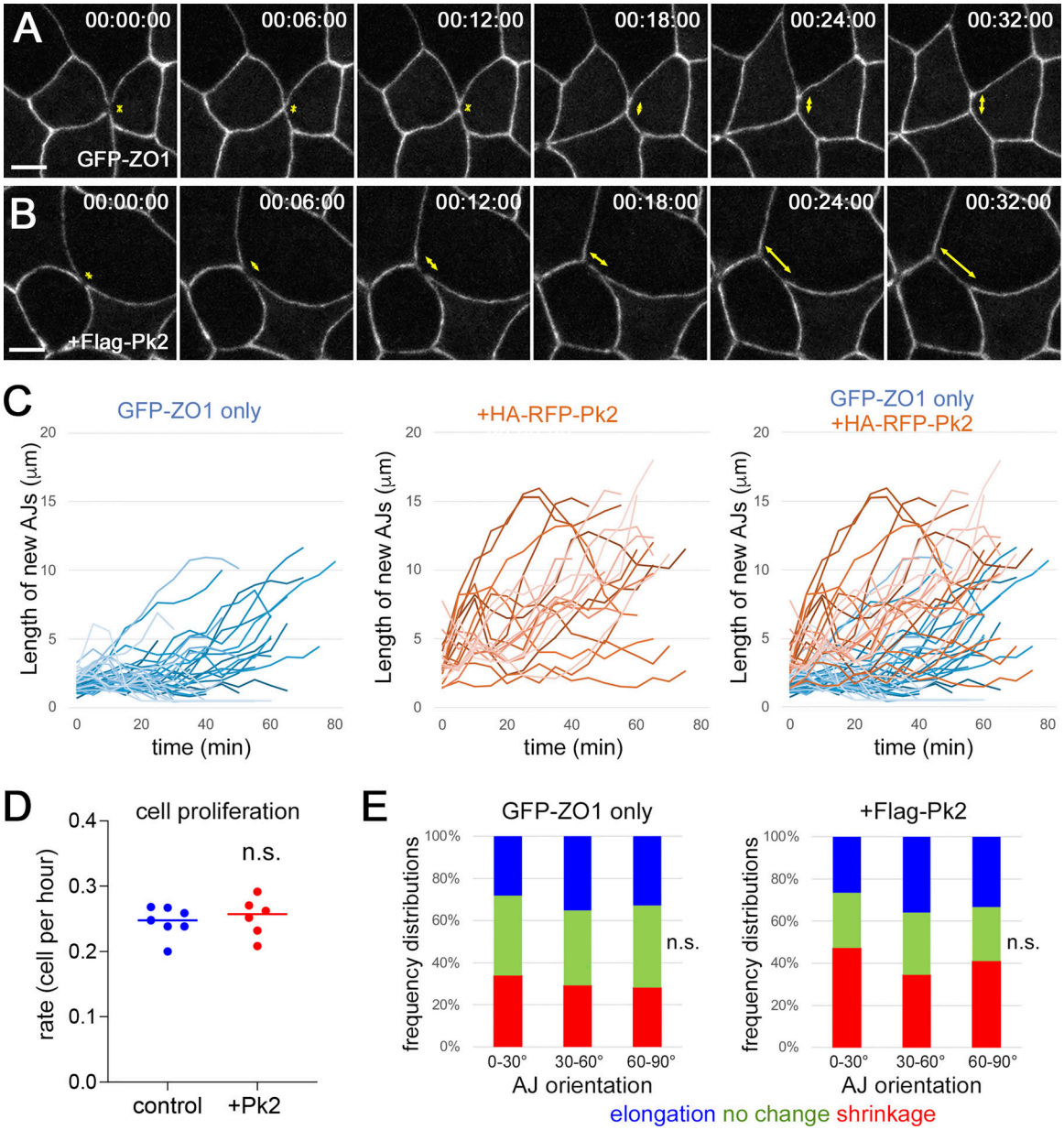


Figure S3. **Pk2 promotes the elongation of newly formed AJs after cytokinesis. (A and B)** Representative snapshot images of new AJ formation after cytokinesis. *Xenopus* gastrula ectoderm expressing GFP-ZO1 only (A) or with Flag-Pk2 (B). Time-lapse imaging was initiated at stage 11, and t = 0 was set at the time when the contractile ring was closed. **(C)** Length changes of newly formed AJs in cells expressing only GFP-ZO1 (blue) or with HA-RFP-Pk2 (red). Three embryos per group were used. The total number of newly formed AJs was as follows: *n* = 38 (control); *n* = 20 (HA-RFP-Pk2). The maximum value of AJ length after cytokinesis was used for statistical analysis. Unpaired Student's *t* test (two-sided). The data distribution was tested for normality using the Kolmogorov–Smirnov normality test. P < 0.0001. **(D)** Cell proliferation rate in stage 10–11.5 embryos expressing GFP-ZO1 only or GFP-ZO1 with Flag-Pk2. The dots represent the average rate of cell proliferation in individual embryos. The lines represent the means of seven (control) or six (+Pk2) embryos. Unpaired Student's *t* test (two-sided). The data distribution was tested for normality using the Kolmogorov–Smirnov normality test. The total number of cells was as follows: *n* = 875 (control); *n* = 853 (Flag-Pk2). **(E)** Quantification of the correlation between AJ length changes and AJ orientation in the control (left) and Pk2 MO (right) gastrula ectoderms. 30 AJs were randomly selected from time-lapse images of three embryos per group. Changes in AJ length were categorized as follows: elongation (blue, ≥0.8 μm/3 min), shrinkage (red, less than or equal to −0.8 μm/3 min), and no change (green, −0.8< and <0.8 μm/3 min). On the basis of orientation, AJs were categorized into AP (≤30° from the AP axis), ML (≤30° from the ML axis), and mid (30–45° from either the AP or ML axes). The two-sample Kolmogorov–Smirnov test was used on original numerical data of AJ length changes. Distributions were compared between AP and ML junctions. Three embryos per group were used. 10 AJs per embryo were used. The total number of AJ length changes was as follows: *n* = 1,258 (control) and *n* = 910 (Pk2 KD). n.s., not significant. Scale bars: 10 μm.

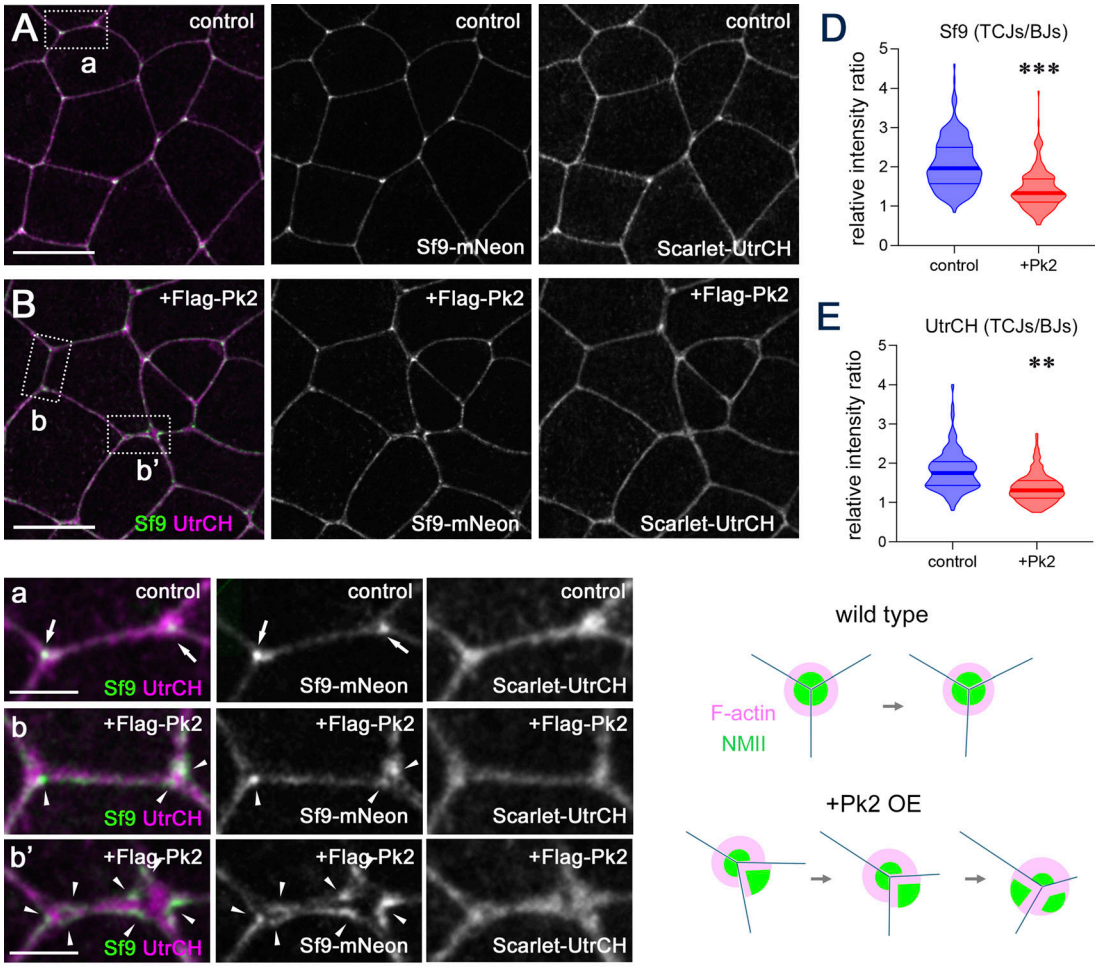


C

| NMII puncta | Control #1 | Control #2 | Control #3 | Pk2 OE #1 | Pk2 OE #2 | Pk2 OE #3 |
|---|---|---|---|---|---|---|
| 1 | 63 (0.9265) | 58 (0.9206) | 69 (0.92) | 33 (0.5690) | 35 (0.5833) | 33 (0.5410) |
| 2 | 5 (0.0735) | 5 (0.0794) | 6 (0.08) | 23 (0.3966) | 20 (0.3333) | 26 (0.4262) |
| 3 | 0 (0) | 0 (0) | 0 (0) | 2 (0.0345) | 5 (0.0833) | 2 (0.0328) |

Figure S4. **Pk2 changes the organization of the actomyosin network at TCJs. (A and B)** Representative images of Sf9-mNeon and Scarlet-UtrCH in the control (A) or Flag-Pk2–expressing (B) gastrula ectoderm. Imaging was initiated at stage 11. The square areas in A and B are enlarged in a, b, and b′. The arrows represent NMII puncta formed near the center of the F-actin puncta in tricellular vertices in the wild-type ectoderm. The arrowheads in b and b′ represent split NMII puncta in the Pk2-overexpressing ectoderm. Schematics are shown in the right panel. Note that some NMII puncta are in the peripheral region of tricellular vertices. **(C)** Number of NMII puncta in individual vertices. Vertices consisting of three cells were used for quantification. Images of sf9-mNeon were processed with a threshold mask (>300 fluorescence intensity). The number of identifiable sf9-mNeonGreen puncta near TCJs was counted. The chi-square test. $P < 0.001$. Three embryos per group were used. The total number of TCJs was as follows: $n = 206$ (control) and $n = 179$ (+Pk2 OE). **(D and E)** Quantification of Sf9-mNeonGreen (D) and Scarlet-UtrCH (E) fluorescence intensity at TCJs. After segmentation, the mean fluorescence intensities were measured via dilated masks of pixels that defined TCJs (five pixels [0.76155 µm] in diameter). The Mann–Whitney U test was used to compare mean ranks. Three embryos per group were used. The total number of TCJs was as follows: $n = 243$ (control) and $n = 195$ (+Flag-Pk2). *P < 0.05; **P < 0.01, ***P < 0.001. Scale bars: 20 µm (A and B) and 5 µm (a–b′).

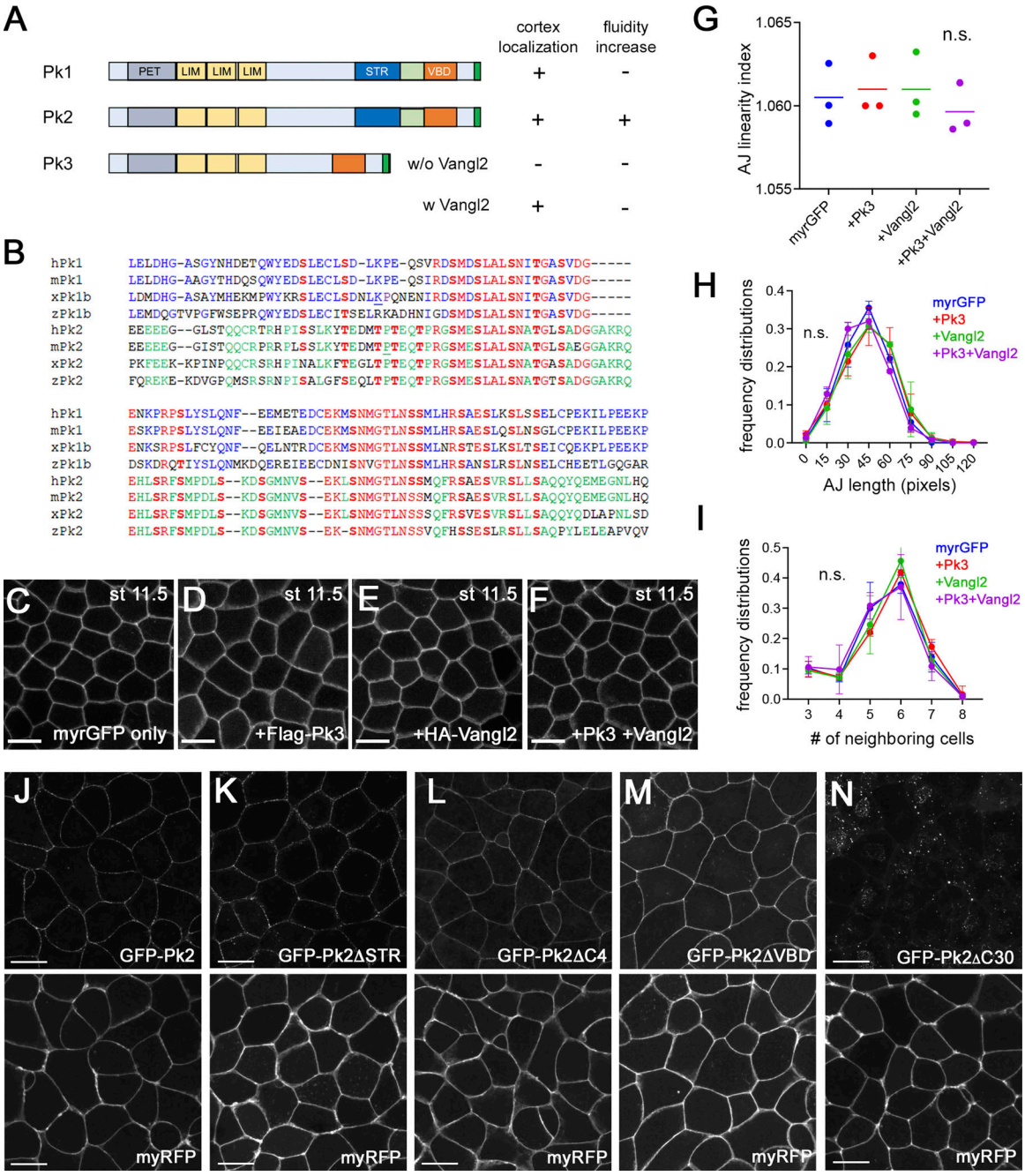


Figure S5. **Neither Pk1 nor Pk3 increases tissue fluidity in the gastrula ectoderm. (A)** Domain structure of Pk1, Pk2, and Pk3. Note that Pk3 does not contain the STR (blue) or C4 (light green) regions. **(B)** Alignment of the STRs of human, mouse, *Xenopus*, and zebrafish Pk1 and Pk2. Conserved amino acids among both Pk1 and Pk2 (red), only Pk1 (blue), or only Pk2 (green). **(C–F)** Representative images of *Xenopus* gastrula ectoderms expressing myrGFP only (C), with Flag-Pk3 (D), with HA-Vangl2 (E), or with Flag-Pk3 and HA-Vangl2 (F). Imaging was initiated at stage 11.5. Pigmented wild-type embryos were used for image acquisition and quantification. **(G–I)** Quantification of cell packing according to the variation in AJ length (G), AJ linearity (H), and the number of neighboring cells (I). Statistical analyses in G and I were based on the original numeric data. One-way ANOVA was used to compare mean ranks, with the Bonferroni correction for multiple pairwise comparisons in G. The Kolmogorov–Smirnov test was used to compare distributions in H. The chi-square test was used in I. Three embryos per group were used. The total number of cells was as follows: 281 cells and 827 AJs (myrGFP only); 191 cells and 578 AJs (Pk3 only); 329 cells and 959 AJs (Vangl2 only); and 368 cells and 1,068 AJs (Pk3 and Vangl2). n.s., not significant. **(J–N)** Subcellular distribution of the GFP-Pk2 mutant protein in the gastrula ectoderm. Representative images of cells expressing GFP-Pk2 (J), GFP-Pk2ΔSTR (K), GFP-Pk2ΔC4 (L), GFP-Pk2ΔVBD (M), or GFP-Pk2ΔC30 (N). Stage 11.5. myrRFP RNA was coinjected to label the plasma membrane. Scale bars: 20 µm.

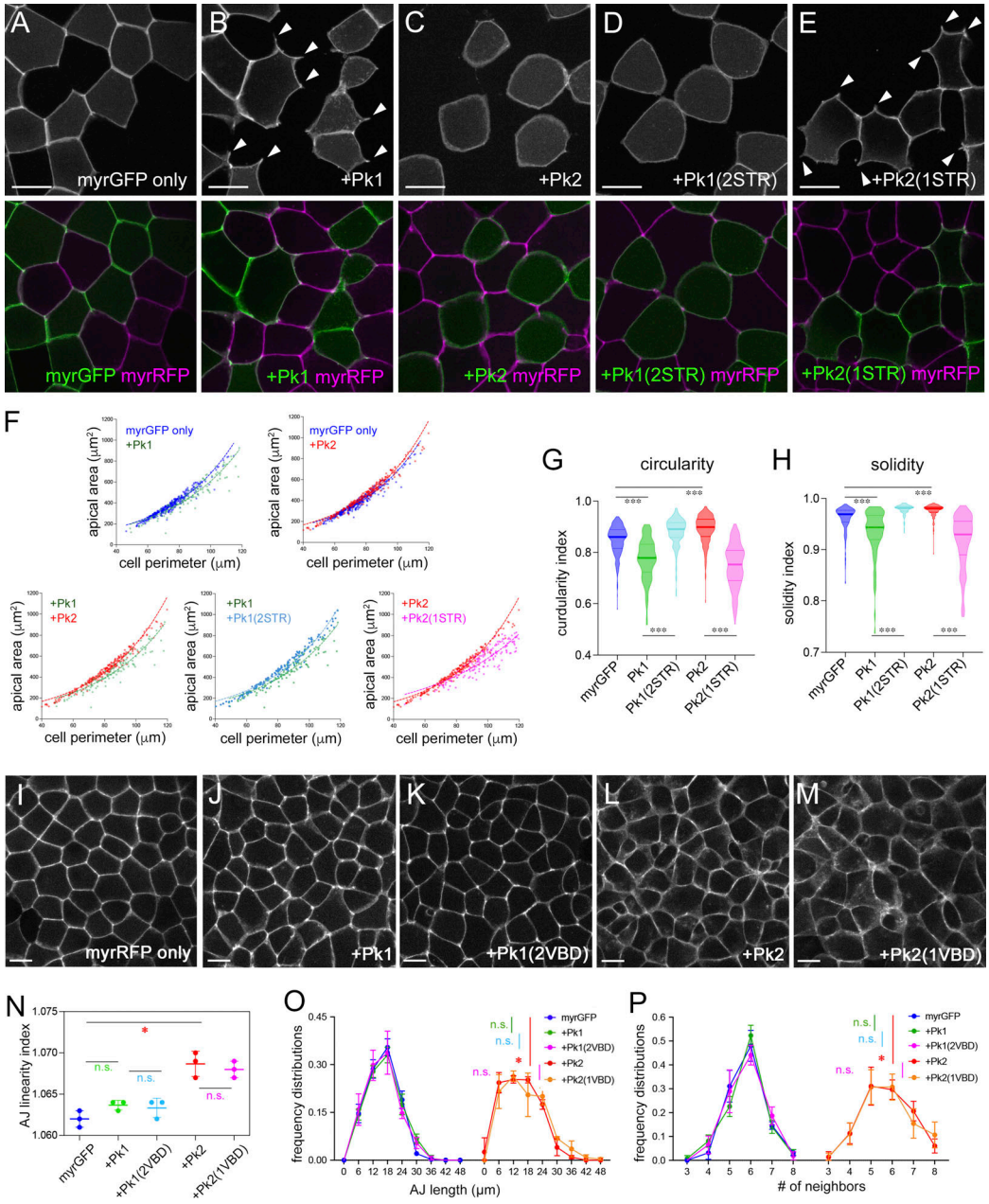


Figure S6. **STR is responsible for the functional difference between Pk1 and Pk2 on AJs and actomyosin. (A–E)** Representative images of *Xenopus* gastrula ectoderms mosaically expressing myrGFP only (A), with HA-Pk1 (B), with Flag-Pk2 (C), with HA-Pk1(2STR) (D), or with Flag-Pk2(1STR) (E). myrGFP and Pk mutant RNA were injected into one ventral-animal blastomere in stage four to eight embryos. myrRFP RNA was injected into the other ventral-animal blastomere to label neighboring cells. Pigmented wild-type embryos were used for image acquisition and quantification. Imaging was initiated at stage 11. **(F)** 2D plots of the cell shapes in A–E. The x axis represents the cell perimeter. The y axis represents the apical domain size. Individual dots represent cells expressing myrGFP only (blue), HA-Pk1 (green), Flag-Pk2 (red), HA-Pk1(2STR) (light blue), or Flag-Pk2(1STR) (purple). Mosaic cells were those that shared cell–cell boundaries with at least three myrRFP-injected cells. **(G and H)** Circularity (G) and solidity (H) of Pk mutant-expressing cells. The same cells in F were used for quantification. An ImageJ plugin, Particle Analyzer, was used for the calculations. Circularity = 4pi (area/perimeter^2). Solidity (convexity) = apical domain size/convex hull area. A maximum value of 1 represents a perfect circle. Cells with <100 μm$^2$ apical domain area were excluded to increase the reliability of the assays. One-way ANOVA was used to compare means, with the Bonferroni correction for multiple pairwise comparisons. Three embryos per group were used. The total number of cells was as follows: 298 cells (myrGFP only); 116 cells (+Pk1); 165 cells (+Pk1(2STR)); 249 cells (+Pk2); 187 cells (+Pk2(1STR)). **(I–M)** Representative images of *Xenopus* gastrula ectoderms expressing myrGFP only (I), with Pk1 (J), with Pk1(2VBD) (K), with Pk2 (L), or with Pk2(1VBD) (M). Imaging was initiated at stage 11.5. Pigmented wild-type embryos were used for image acquisition and quantification. **(N–P)** Quantification of hexagonal cell packing according to the variation in AJ linearity (N), AJ length (O), and the number of neighboring cells (P). The dots indicate the average AJ linearity in individual embryos. The lines indicate the average AJ linearity of three embryos. Statistical analyses of N and O were based on the original numeric data. One-way ANOVA was used to compare means, with the Bonferroni correction for multiple pairwise comparisons in N. The Kolmogorov–Smirnov test was used to compare distributions in O. The chi-square test was used in P. Three embryos per group were used. The total number of cells and AJs was as follows: 123 cells and 409 AJs (myrGFP only); 123 cells and 374 AJs (+Pk1); 100 cells and 366 AJs (+Pk1(1VBD)); 115 cells and 355 AJs (+Pk2); and 146 cells and 290 AJs (+Pk2(1VBD)). *P < 0.05, **P < 0.01, ***P < 0.001, n.s., not significant. Scale bars: 20 μm.

Video 1. **Representative time-lapse video showing the dynamics of NE cells during NTC in Pk2-KD embryos.** Pk2 MO was coinjected with RNA encoding Lifeact-GFP in one dorsal blastomere at the four- to eight-cell stage, and RNA encoding Scarlet-UtrCH was injected into the other dorsal blastomere. The posterior NE near the border between the head and the spinal cord was imaged from the dorsal side (dorsal view, as shown in Fig. 1 A). Time-lapse imaging was initiated at stage 14 with 5-min interval. The time-lapse duration was 3 h 40 min at room temperature.

Video 2. **Representative time-lapse video of the control (left) and Pk2-depleted NEs (right).** Scarlet-UtrCH was injected into one dorsal blastomere. Pk2 MO was coinjected with Lifeact-GFP in the other dorsal blastomere. The circles represent T1 junctions. Dorsal view imaging was initiated at stages 15–16 with 3-min intervals. The time-lapse duration was 1 h 12 min at room temperature.

Video 3. **Representative time-lapse video showing changes in cell orientation (green lines) in control NEs and Pk2-KD NEs.** Pk2 MO was coinjected with RNA encoding myrGFP in one dorsal blastomere at the four- to eight-cell stage. RNA encoding myrRFP was injected into the other dorsal blastomere. Dorsal view imaging was initiated at stages 15–16 with 3-min intervals. The time-lapse duration was 1 h 12 min at room temperature.

Video 4. **Representative time-lapse video of the Pk1 morphant NE.** Pk1 MO was coinjected with Lifeact-GFP in one dorsal blastomere. Dorsal view imaging was initiated at stages 15–16 with 5-min intervals. The time-lapse duration was 1 h 45 min at room temperature.

Video 5. **Representative time-lapse video of the NE expressing Scarlet-UtrCH and sf9-mNeonGreen, which are live probes for F-actin and NMII.** The wild-type control NE (top) and the Pk2 KD NE (bottoms). Scarlet-UtrCH and sf9-mNeonGreen RNA were coinjected into one dorsal blastomere. The white arrowheads represent sf9 enrichment at T1 junctions. Dorsal view imaging was initiated at stages 14–15 with 3-min intervals. The time-lapse duration was 1 h 21 min at room temperature.

Video 6. **Representative time-lapse video showing hexagonal packing during gastrulation in wild-type (left) and Flag-Pk2 OE (right) embryos.** RNA encoding myrGFP was injected with or without Flag-Pk2 RNA into two ventral blastomeres of four-cell-stage embryos. The animal-side ectoderm was imaged from the top of the embryos, and albino embryos were used. Time-lapse imaging was initiated at stage 10 with 5-min intervals. The time-lapse duration was 4 h 55 min at room temperature.

Video 7. **Representative time-lapse video showing hexagonal packing and lateral domain dynamics in the control wild-type (left) and Flag-Pk2 OE (right) ectoderms.** Injection was performed as described in Fig. 3 A. The animal-side ectoderm was imaged at stage 11.5 with 5-min intervals. Albino embryos were used. The time-lapse duration was 1 h 45 min at room temperature.

Video 8. **Representative time-lapse video showing YFP-C-cadherin dynamics in the control wild-type (left) and Flag-Pk2 OE (right) ectoderms.** RNA encoding C-cadherin-YFP was injected into two ventral blastomeres of four-cell-stage embryos with or without RNA encoding Flag-Pk2. The animal-side ectoderm was imaged. Time-lapse imaging was initiated at stage 11 with 30-s intervals. The time-lapse duration was 14 min 30 s at room temperature.

Video 9. **Representative time-lapse video showing the dynamics of F-actin and NMII at TCJs.** sf9-mNeonGreen and Scarlet-UtrCH RNA were injected with or without Flag-Pk2 RNA into two ventral blastomeres. Top panels: control. Bottom panels: +Flag-Pk2. Animal view time-lapse imaging starts at stage 11. The time-lapse durations were 39 min 30 s at room temperature with 30-s intervals.

Video 10. **Representative time-lapse video showing the dynamics of NE cells expressing high levels of Flag-Pk2 (left panel), HA-Pk1 (middle panel), or HA-Pk1(2STR) (right panel).** RNA encoding Scarlet-UtrCH was injected into one dorsal blastomere of a four-cell-stage embryo (purple on the left side of the NE). RNAs encoding Lifeact-GFP and various Pk constructs were coinjected into the other dorsal blastomere. Dorsal view time-lapse imaging was initiated at stage 14. The time-lapse duration was 2 h 36 min at room temperature with 6-min intervals.